Black Hole Mass Scaling Relations for Early-type Galaxies. I. M_{BH}–$M_{*,sph}$ and M_{BH}–$M_{*,gal}$

Nandini Sahu[1,2] , Alister W. Graham[2] , and Benjamin L. Davis[2]

[1] OzGrav-Swinburne, Centre for Astrophysics and Supercomputing, Swinburne University of Technology, Hawthorn, VIC 3122, Australia; nsahu@swin.edu.au
[2] Centre for Astrophysics and Supercomputing, Swinburne University of Technology, Hawthorn, VIC 3122, Australia

Abstract

Analyzing a sample of 84 early-type galaxies (ETGs) with directly measured supermassive black hole masses—nearly doubling the sample size of such galaxies with multicomponent decompositions—a symmetric linear regression on the reduced (merger-free) sample of 76 galaxies reveals $M_{BH} \propto M_{*,sph}^{1.27\pm0.07}$ with a total scatter of $\Delta_{rms} = 0.52$ dex in the $\log(M_{BH})$ direction. Importantly, however, we discover that the ES/S0-type galaxies with disks are offset from the E-type galaxies by more than a factor of ten in their $M_{BH}/M_{*,sph}$ ratio, with ramifications for formation theories, simulations, and some virial factor measurements used to convert AGN virial masses into M_{BH}. Separately, each population follows a steeper relation with slopes of 1.86 ± 0.20 and 1.90 ± 0.20, respectively. The offset mass ratio is mainly due to the exclusion of the disk mass, with the two populations offset by only a factor of two in their $M_{BH}/M_{*,gal}$ ratio in the M_{BH}–$M_{*,gal}$ diagram where $M_{BH} \propto M_{*,gal}^{1.8\pm0.2}$ and $\Delta_{rms} = 0.6 \pm 0.1$ dex depending on the sample. For $M_{BH} \gtrsim 10^7 M_\odot$, we detect no significant bend nor offset in either the M_{BH}–$M_{*,sph}$ or M_{BH}–$M_{*,gal}$ relations due to barred versus non-barred, or core-Sérsic versus Sérsic, ETGs. For reference, the ensemble of late-type galaxies (which invariably are Sérsic galaxies) follow M_{BH}–$M_{*,sph}$ and M_{BH}–$M_{*,gal}$ relations with slopes equal to 2.16 ± 0.32 and 3.05 ± 0.70, respectively. Finally, we provide some useful conversion coefficients, υ, accounting for the different stellar mass-to-light ratios used in the literature, and we report the discovery of a local, compact massive spheroid in NGC 5252.

Key words: black hole physics – galaxies: bulges – galaxies: elliptical and lenticular, cD – galaxies: evolution – galaxies: photometry – galaxies: structure

Supporting material: figure set

1. Introduction

There is growing evidence suggesting that black holes exist in a continuum of masses, from stellar mass black holes (a few $M_\odot$ to ~$100 M_\odot$; Belczynski et al. 2010; Abbott et al. 2016) to supermassive black holes (SMBHs) ($10^5 M_\odot$–$10^{10} M_\odot$; Lynden-Bell 1969; Wolfe & Burbidge 1970; Lynden-Bell & Rees 1971; Natarajan & Treister 2009; Inayoshi & Haiman 2016). In between these two mass ranges lie the intermediate-mass black holes (Miller 2003; Mapelli 2016; Mezcua 2017; Graham et al. 2019, and references therein). A galaxy may contain several thousand (Hailey et al. 2018) to millions (Elbert et al. 2018) of stellar-mass black holes, but typically only one central SMBH; there are many theories as to why this is so (Miller 2003; Mayer et al. 2007; Hirano et al. 2017; Morganti 2017).

In order to gain insight and improve these theories, for the last three decades, astronomers have been investigating the underlying relations between SMBHs and various properties of the host galaxies (see the review in Graham (2016), and references therein). Based on the work in Dressler (1989), as well as various black hole formation scenarios and feedback models, most astronomers have come to envision a fundamental scaling relation existing between the mass of an SMBH and that of the spheroidal stellar component of the host galaxy.

Building on some of the previous estimates of black hole masses, Dressler & Richstone (1988) predicted an upper limit of $10^9 M_\odot$ for the central SMBH mass of the galaxies with the largest spheroids. Their prediction was based on the central black hole mass (M_{BH}) and spheroid stellar mass (M_{sph} or

M_{bulge}) ratios in the two neighboring galaxies M31 and M32. Dressler (1989) directly—and Yee (1992) indirectly—suggested a linear relationship between the black hole mass and bulge mass of a galaxy. Kormendy & Richstone (1995) and Magorrian et al. (1998) subsequently observed a linear relation between M_{BH} and M_{bulge}.

Using larger samples of galaxies and updated black hole masses, most astronomers continued to report a near-linear M_{BH}–M_{bulge} relation for nearly two decades (e.g., Ho 1999; Ferrarese & Ford 2005; Graham 2007b; Gültekin et al. 2009a; Sani et al. 2011). However, during the same period, some astronomers (Laor 1998; Wandel 1999) found a steeper relation due to the addition of low-mass galaxies in their data sets. Salucci et al. (2000) reported that spiral galaxies have a steeper M_{BH}–M_{bulge} slope than massive elliptical galaxies. Further, Laor (2001) reported $M_{BH} \propto M_{bulge}^{1.53\pm0.14}$ based on his work with an updated sample of 40 quasars.

Graham (2012) observed two different slopes in the M_{BH}–L_{bulge} diagram for galaxies with Sérsic or core-Sérsic spheroids (Graham et al. 2003). He found a near-linear M_{BH}–L_{bulge} relation for the massive core-Sérsic galaxies (all of which were early-type galaxies (ETGs)), and a "super-quadratic"[3] relation for the low-mass Sérsic galaxies (most of which were late-type galaxies (LTGs)). Further, Graham & Scott (2013) and Scott et al. (2013), with their work on a larger sample of galaxies, recovered this bent relation, and Graham & Scott (2015) showed that the so-called pseudobulges

---

[3] The phrase "super-quadratic" was used to describe a power-law with a slope greater than two but not as steep as three.

(Gadotti & Kauffmann 2009; Kormendy et al. 2011) also complied with the nonlinear (super-quadratic) arm of the bent relation. The bent relation strongly suggested the need to revisit various theories and implications based on the previously assumed linear relation. For example, if there is evolution along the M_{BH}–M_{sph} relation, then the steeper relation reveals that the fractional growth of a black hole's mass is faster than that of low-mass spheroids (Sérsic galaxies), consistent with many other works (e.g., Diamond-Stanic & Rieke 2012; Seymour et al. 2012; LaMassa et al. 2013; Drouart et al. 2014).

These M_{BH} scaling relations will help us understand the rate at which the black hole mass grows relative to the star formation rate in the host galaxy, which further aids formation and evolution theories regarding black holes and the galaxies that encase them (e.g., Shankar et al. 2009). This also helps to further our understanding of AGN feedback models between a SMBH and its host galaxy (e.g., Hopkins et al. 2006). In the past, some simulations have reported steeper (at the low-mass end) and bent M_{BH}–$M_{*,sph}$ relations (Cirasuolo et al. 2005; Fontanot et al. 2006; Dubois et al. 2012; Khandai et al. 2012; Bonoli et al. 2014; Neistein & Netzer 2014; Anglés-Alcázar et al. 2017), which partly supports our findings.

Gadotti & Kauffmann (2009) reported discrepancies between the black hole mass estimated from the M_{BH}–σ relation and the single linear M_{BH}–$M_{*,sph}$ relation for all types of (elliptical, lenticular, and spiral) galaxies. There are, in fact, many influential works that have based their predictions on a single linear M_{BH}–$M_{*,sph}$ relation, for all types of galaxies (Fabian 1999; Wyithe & Loeb 2003; Marconi et al. 2004; Begelman & Nath 2005; Springel et al. 2005; Croton et al. 2006; Di Matteo et al. 2008; Natarajan & Volonteri 2012). This can affect the inferred science; hence we recommend that these simulations be revisited using the new scaling relations.

Numerous investigations of the M_{BH}–M_{sph} relation have been based on the belief that there is a strong possibility that the black hole mass correlates better with its host bulge stellar mass, rather than with its host galaxy (or total) stellar mass, reflected by the smaller scatter in the M_{BH}–M_{sph} relation. However, Läsker et al. (2014)[4] have claimed, based on their ETG-dominated sample of 35 galaxies, that black hole mass correlates equally well with total galaxy luminosity as it does with the bulge luminosity. Additionally, there have been several detections of bulgeless galaxies harboring massive black holes at their center (e.g., Reines et al. 2011; Secrest et al. 2012; Schramm et al. 2013; Simmons et al. 2013; Satyapal et al. 2014). This suggests the possibility of the black hole mass correlating directly with the galaxy mass (M_{gal}), whether this be the stellar, baryonic, or total mass (Ferrarese 2002; Baes et al. 2003; Sabra et al. 2015; Davis et al. 2018a).

Recent work by Savorgnan et al. (2016) used a larger sample of 66 galaxies—consisting of 47 ETGs and 19 LTGs—and reported that black hole mass only correlates equally well with bulge luminosity and total galaxy luminosity for ETGs, but not for LTGs (see their Figures 1 and 2). They also suggested a different idea for the bend in the M_{BH}–M_{sph} relation that was not detected by Läsker et al. (2014). For the core-Sérsic and Sérsic galaxies in Savorgnan et al. (2016), they found $M_{BH} \propto M_{*,sph}^{1.19\pm0.23}$ and $M_{BH} \propto M_{*,sph}^{1.48\pm0.20}$, respectively. The slopes for these two populations have overlapping uncertainties (within the 1σ level). Unlike the case in Scott et al. (2013),

where the bulge masses were estimated using a morphologically dependent bulge-to-total ratio for 75 late- and early-type galaxies, here there is no clear bend. Furthermore, Savorgnan et al. (2016) found different trends for their ETGs and LTGs, which they refer to as a "red sequence" and a "blue sequence," respectively, although color information is not shown in that diagram.

Our work on the hitherto largest data set of 84 ETGs, with directly measured black hole masses, builds on Savorgnan & Graham (2016a) and nearly doubles their number of ETGs with multicomponent decompositions. ETGs consist of ellipticals (E), elliculars[5] (ES), and lenticulars (S0), where the latter two types have disks. Ellicular and lenticular galaxies often contain bars, bar-lenses, inner disks, rings, and ansae in addition to the bulge and disk. ETGs are often misclassified because many catalogs, e.g., the Third Reference Catalogue of Bright Galaxies (RC3) (de Vaucouleurs et al. 1991), failed to identify disks from a visual inspection of the images. For our set of ETGs, we perform multicomponent decompositions to identify disks and bars, and to separate the bulge luminosity from the total galaxy luminosity. We intend to refine how the black hole mass correlates with its host spheroid stellar mass, and to determine how it correlates with the host galaxy stellar mass. We investigate whether or not the core-Sérsic and Sérsic galaxies cause the bend in the M_{BH}–M_{sph} relation. We also combine our work on ETGs with the study of LTGs by Davis et al. (2018a, 2019), in order to further explore the reason behind the bend in the M_{BH}–M_{sph} relation. Furthermore, we explore the possibility of different M_{BH}–M_{sph} relations depending on the ETG submorphology; i.e., for galaxies with and without a disk, and galaxies with and without a bar. In all the cases, we also investigate the prospect of a better or equally likely correlation of black hole mass with total galaxy stellar mass.

In Section 2, we describe our imaging data set and primary data reduction techniques. Section 3 illustrates the galaxy modeling and multicomponent decomposition of the galaxy light. That section also presents a detailed discussion of the stellar mass-to-light ratios we applied to the luminosity to determine the stellar masses. We compare the masses of the galaxies calculated using different (color-dependent) stellar mass-to-light ratios, and we provide a conversion coefficient that can be applied to bring them into agreement with alternate prescriptions for the mass-to-light ratio. In Section 4, we present the black hole scaling relations for our ETG sample, along with an extensive discussion of the nature of the M_{BH}–$M_{*,sph}$ and M_{BH}–$M_{*,gal}$ relations for various cases: Sérsic and core-Sérsic galaxies, galaxies with and without a disk, galaxies with and without a bar, and ETGs versus LTGs. Finally, in Section 5, we summarize our work and present its main implications. Henceforth, we will be using the terms "spheroid" and "bulge" of a galaxy interchangeably.

2. Imaging Data

We have compiled an exhaustive (current) sample of all 84 ETGs having a directly measured SMBH mass. We use the black hole masses measured from direct methods, i.e., modeling of stellar and gas dynamics. Gas-dynamical modeling is fundamentally simpler: because gases are viscous, they easily settle down and rotate in a circular disk-like structure. Stellar dynamical

---

[4] Läsker et al. (2014) had only four LTGs in their sample.

[5] ETGs with intermediate stellar disks (Liller 1966; Graham et al. 2016a).

modeling, however, is complex and computationally expensive (Walsh et al. 2013). Although both have their pros and cons, we prefer to use the black hole masses measured from stellar dynamics, as stars are influenced only by gravitational forces, while gas dynamics are more prone to nongravitational forces. In order to know more about the aforementioned primary methods of black hole mass measurement, readers are directed to the review by Ferrarese & Ford (2005).

Out of a total of 84 ETGs, we obtain SMBH masses, distances, and light profile component parameters for 40 galaxies from Savorgnan & Graham (2016a). For NGC 1271 and NGC 1277, we directly used the SMBH masses, as well as the bulge and total galaxy stellar masses, from the work on their H- and V-band *Hubble Space Telescope* (*HST*) images respectively retrieved and reduced by Graham et al. (2016a, 2016b). The remaining 42 galaxies were modeled by us, including seven galaxies (A3565 BCG, NGC 524, NGC 2787, NGC 1374, NGC 4026, NGC 5845, and NGC 7052) from the data set of Savorgnan & Graham (2016a) that we remodeled. About 80% of the galaxy images used in this work are *Spitzer Space Telescope* (*SST*) 3.6 μm images taken with the Infra-Red Array Camera (IRAC). The remaining few images are Sloan Digital Sky Survey (SDSS) (York et al. 2000) r'-band images and Two Micron All Sky Survey (2MASS) (Jarrett et al. 2003) K_s-band images.

2.1. Image Sources

IRAC 3.6 μm images (IRAC1) are unaffected by dust absorption, have large fields of view, and are sufficiently spatially resolved to enable us to visually identify the primary galaxy components, thereby increasing the accuracy with which galaxy images are disassembled. Hence, for our analysis, we preferred to use IRAC 3.6 μm images. However, for some galaxies whose *Spitzer* images are not available, we used images from the SDSS archive and 2MASS catalog.

The 42 galaxy images that we modeled (including the seven we remodeled) were comprised of 33 images in the 3.6 μm band, out of which five images were downloaded from the *Spitzer* Survey of Stellar Structure in Galaxies (S^{4}G) pipeline-1 (Sheth et al. 2010; Muñoz-Mateos et al. 2013; Querejeta et al. 2015), and 28 images were obtained from the *Spitzer* Heritage Archive (SHA) (Levine et al. 2009; Wu et al. 2010; Capak et al. 2013). Of the remaining nine galaxies, six K_s-band images were obtained from 2MASS (Jarrett et al. 2003) and three r'-band images are from the SDSS Data Release-8 (Aihara et al. 2011).

Images from the S^{4}G pipeline-1 (P1)[6] are science-ready, calibrated images formed by mosaicking individual Basic Calibrated Data (BCD) frames. The S^{4}G survey is limited to galaxies with a maximum distance of 40 Mpc, a B-band apparent magnitude brighter than 15.5 mag, and a size limit $D_{25} > 1'$ (Sheth et al. 2010). We obtained 3.6 μm images of galaxies not fitting these criteria from SHA; these are level-2, post-Basic Calibrated Data (pBCD)[7] images. The pBCD images are a mosaicked form of level-1 corrected Basic Calibrated Data (cBCD) frames. Level-1 cBCD frames have already undergone dark current subtraction, flat-field correction, various instrument artifact corrections, and flux calibration.

Table 1
Photometric Parameters

Image Source	Zero-point (mag[a])	Pixel Scale ($''$)	Υ_* ($M_\odot/L_\odot$)	MAG$_\odot$ (mag)
S4G	21.097[b]	0.75	0.6[f]	6.02
SHA	21.581[c]	0.6	0.6[f]	6.02
2MASS	Image specific[d]	1	0.7[g]	5.08
SDSS	22.5[e]	0.4	2.8[h]	4.65

Notes. Columns: (1) Image source. (2) Photometric zero-points of images in AB magnitude. (3) Pixel size of images. (4) Stellar mass-to-light ratios used to convert measured luminosities into stellar masses. (5) Absolute magnitude of Sun in AB magnitude system.
[a] AB magnitude system.
[b] Salo et al. (2015), their Equation (13).
[c] Muñoz-Mateos et al. (2016), their Equation (1).
[d] Zero-points specified in image headers were converted from Vega magnitude to AB magnitude using Equation (5) from Blanton et al. (2005).
[e] Blanton et al. (2005), their Equation (4).
[f] Taken from Meidt et al. (2014) for 3.6 μm band.
[g] Using $\Upsilon_*^{3.6}$ in the equation $\Upsilon_*^{3.6\,\mu m} = 0.92 \times \Upsilon_*^{K_s} - 0.05$ from Oh et al. (2008).
[h] Calibrated using $\Upsilon_*^{r'} = \Upsilon_*^{K_s} \times L_{K_s}/L_{r'}$ with $\Upsilon_*^{K_s} = 0.7$.

The r'-band images of three galaxies (NGC 6086, NGC 307, and NGC 4486B) from the SDSS catalog are also undergone basic correction and calibration. Although optical-band images suffer from dust extinction, our choice of SDSS images is justified because they have a large field of view and sufficient resolution to help us identify galaxy components. For the remaining six galaxies (A1836 BCG, Mrk 1216, NGC 1550, NGC 4751, NGC 5328, and NGC 5516), we used flux-calibrated[8] K_s-band images from the 2MASS catalog.

About 95% of the images in our total galaxy sample of 84 are in either the 3.6 μm (roughly L-band) or the 2.17 μm (K_s-band), which helps us obtain a more reliable distribution and measurement of luminosity and stellar mass, due in part to a stable stellar mass-to-light ratio in these bands (described in Section 3.3). Table 1 lists the flux calibration zero points, image pixel scale, stellar mass-to-light ratios used in this work, and solar absolute magnitude in different image pass-bands.

2.2. Image Reduction and Analysis

All the images obtained from the various telescope pipelines described above have already undergone dark current subtraction, flat-fielding, bad pixel and cosmic ray correction, sky-subtraction (except for S^{4}G and 2MASS images), and flux calibration. The automated routines in the telescope pipelines either over- or underestimated the sky-background intensity, which we observed for most of our galaxies. Hence, we started our image analysis by measuring the sky-background intensities, generating the image masks, and calculating the telescope's point-spread function (PSF).

2.2.1. Sky Backgrounds

Sky-background level subtraction is a crucial step in accurately measuring a galaxy's luminosity. As our target galaxy images are extended over a large number of pixels in the CCD images that we are using, an error in sky background
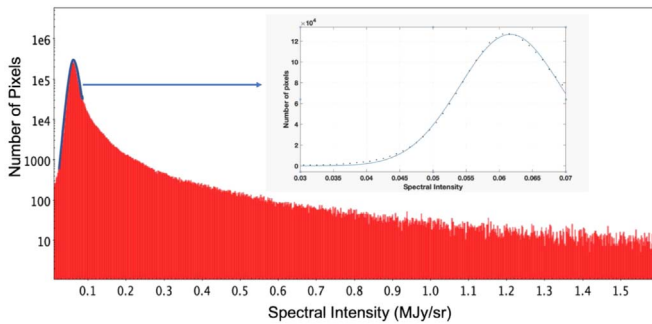
Figure 1. Gaussian fit to the sky-background intensity of the level-2 corrected, 3.6 μm band image of NGC 1600 from SHA. It has already undergone sky subtraction, but the sky level peaking at a nonzero value indicates that it still requires adjustment. The red distribution shows the faint (sky-dominated) end of the intensity histogram (number of pixels at each intensity value) from the CCD image of NGC 1600. The inset plot shows a Gaussian fit (blue curve) to the sky values in the range of 0.03–0.07 MJy/sr, peaking at 0.062 MJy/sr. The intensity distribution following the peak includes the intensity of our target galaxy and other radiating sources (added with the sky value).

intensity subtraction will lead—especially at larger radii—to a systematic error in the surface brightness profile. At large radii, it will result in an erroneous measurement of the luminosity of galaxy components, which in turn will affect the inner components and the total galaxy luminosity. The wide-field images that we obtained from the SHA and SDSS pipelines have already undergone sky subtraction, but as we analyzed the intensity distribution of the images, we found that the peak of the sky-background level was offset from zero for almost all of the images. Hence, it was necessary to calculate the correction in order to tune the sky level of these images to zero.

To calculate the sky-background intensity level, we follow a procedure similar to the one explained in Almoznino et al. (1993). The intensity distribution of the sky-background photons incident on a CCD image ideally follows a Poisson distribution when the only source of systematic error is random emission from the radiating object—in this case, the sky background. However, many other systematic errors are introduced in a CCD image when it undergoes telescope pipelining. In that case, a Gaussian distribution (normal distribution) can be a better approximation for the intensity distribution of the sky background. We constructed the intensity function (pixel number of given intensity versus intensity histogram) of the entire image frame (not just a few portions of the sky that appear free of sources) and fit a Gaussian to the portion of the histogram dominated by the sky (the peak at lower-intensity values), as shown in Figure 1. Intensity values of the pixels occupied by other radiating sources, including our target galaxy, produce the long tail toward higher intensities. The Gaussian fit gives us an optimally accurate mean sky value and the standard deviation (rms error) in any one pixel.

2.2.2. Masking

Images for our galaxy sample have large fields of view. Apart from our target galaxy, these images also contain other radiating sources around and overlapping with the target galaxy. Major contaminating sources are background quasars and foreground stars that overlap the pixel area occupied by the galaxy of interest. Hence, for an accurate measurement of the galaxy luminosity, we eliminate the contribution of these

contaminating sources by generating a mask file. A mask is either a .fits or .pl file marking (with their pixel coordinates and pixel size) the areas and sources to be discarded during the analysis.

We used the task MSKREGIONS in the Image Reduction and Analysis Facility (IRAF) software to read a list of user-specified regions to be masked in our image. The task then generates a mask file (.pl or .fits file) using our galaxy image as a reference for the size of the mask file. The list of contaminating objects and subsequent masks is generated in two parts by us:

1. SOURCE EXTRACTOR (Bertin & Arnouts 1996): A threshold background value is used to automatically identify all the objects present in an image and makes a catalog of them, designating each object by its physical coordinates in the image. We can identify and remove our target galaxy from this list (knowing its physical coordinates) and generate a mask file using this catalog via the task MSKREGIONS.
2. MANUAL MASKING: SOURCE-EXTRACTOR cannot identify the background and foreground objects overlapping with the pixel area of our target galaxy. However, it is important to mask them in order to avoid biasing the image decomposition; therefore, we need to mask them manually. We carefully find the overlapping sources by observing our galaxy at different brightness (contrast) levels. For this purpose, we use the astronomical imaging and data visualization application SAOIMAGE DS9. We generate the second mask file of contaminating objects with the MSKREGION task.

We combine the above two mask files using the IMARITH task in IRAF and further use the final mask as a reference for avoiding the contaminated pixels during extraction and modeling of the target galaxy light. Extra care was taken to manually mask dust in the three SDSS r'-band images.

2.2.3. PSF Determination

The spatial resolution of an image is limited by the telescope's aperture size, the wavelength of observation, the pixel size of its instrument, and the atmospheric blurring for ground-based observations. A distant star is a point source whose light profile is ideally described by a delta function. However, due to the collective resolution limitations, it is imaged as an extended object, and its light profile becomes a function with a nonzero width. Hence, the Full Width at Half Maximum (FWHM) of the light profile of a star in an image is a measure of the total *seeing effect*, which is quantified by the PSF of the telescope.

The image of an object obtained by a telescope can be mathematically described as a convolution of its actual profile with the telescope's PSF. Hence, in order to measure the parameters of the actual light (or surface brightness) profile of a galaxy and its components, we need our fitting functions to be convolved with the telescope's PSF.

Moffat (1969) describes how the wings of the seeing profile (PSF) of a telescope are represented better by a Moffat function rather than a Gaussian function. A Moffat function has the mathematical form

$$I(R) = I_0\left(1 + \left(\frac{R}{\alpha}\right)^2\right)^{-\beta}, \qquad (1)$$

where α is the width parameter and β controls the spread in the wings of the seeing profile (see Figure 3 in Moffat 1969). The parameters α and β are related to the FWHM of the profile through the equation FWHM $= 2\alpha\sqrt{2^{\frac{1}{\beta}} - 1}$. The values of α and β increase with poor seeing (e.g., higher atmospheric turbulence), and the profile that they describe gradually approaches a Gaussian. We used the IRAF task IMEXAMINE to determine the PSF of our images. The IMEXAMINE task fits the radial profile of selected stars with a Moffat function and provides the required parameters: FWHM and β.

3. Modeling and Decomposing the Galaxy Light

The luminosity of a galaxy is modeled by fitting quasi-elliptical isophotes[9] at each radius along the semimajor axis (R_{maj}). Ciambur (2016) and Savorgnan & Graham (2016a) each employ both 1D (one-dimensional) and 2D (two-dimensional) modeling and provide a critical comparison of the two techniques. Savorgnan & Graham (2016a) had more success modeling the galaxies as a set of 1D profiles. Hence, we also prefer to use 1D profile modeling, which takes into account the radial variation in all of the isophotal parameters, such as ellipticity (ϵ), position angle (PA), and the irregularity in an isophote's shape across the whole 2π azimuthal range as quantified using Fourier harmonic coefficients. Therefore, 1D modeling should not be confused with the light profile obtained only from a one-dimensional cut of a galaxy image.

ETGs are commonly ill-considered to be featureless (no subcomponents) and are expected to have regular elliptical isophotes, a scenario that is only valid for purely elliptical galaxies. ETGs can be morphologically subclassified as ellipticals (E) consisting of an extended spheroid, elliculars (ES) consisting of an extended spheroid with an intermediate-scale disk (e.g., Graham et al. 2016a), and lenticulars (S0) comprised of a spheroid and an extended large-scale disk. Apart from these standard components, ETGs may also contain nuclear disks, inner rings, bars, bar-lenses (Sandage 1961; Laurikainen et al. 2009; Saha et al. 2018), outer rings, and ansae (Martinez-Valpuesta et al. 2007; Saha et al. 2018), which can cause nonelliptical or irregular isophotes in a galaxy.

3.1. One-dimensional Representation of the Galaxy Light

We use the new IRAF tasks ISOFIT and CMODEL (Ciambur 2015) to extract the 1D light profile and associated parameter profiles (e.g., ellipticity, PA, etc.), and create a 2D model of each galaxy. ISOFIT and CMODEL are upgraded versions of the IRAF tasks ELLIPSE and BMODEL (Jedrzejewski 1987a, 1987b), respectively.

In order to extract a galaxy light profile, ISOFIT reads a 2D image of a galaxy, as well as the associated mask file, and fits quasi-elliptical isophotes at each radius of the galaxy, from its photometric center to its apparent edge, thus including every part of the galaxy. Further, ISOFIT uniformly samples each isophote across the whole azimuthal range, using a natural angular coordinate for ellipses known as the "Eccentric Anomaly" (ψ) (for more details, see Section 3 of Ciambur (2015)), and provides the average intensity and associated parameters of the isophotes as a function of semimajor axis radii. The isophotal intensity can be expressed in terms of the

average intensity $\langle I_{ell} \rangle$ and Fourier perturbations such that

$$I(\psi) = \langle I_{ell} \rangle + \sum_n [A_n \sin(n\psi) + B_n \cos(n\psi)] \qquad (2)$$

where A_n and B_n are nth-order Fourier harmonic coefficients.

As explained by Ciambur (2015), ISOFIT calculates A_n and B_n while fitting each isophote. These Fourier coefficients, when added together, account for the irregular isophotal shapes and give a near-perfect fit. Ciambur (2015) also mentions that the value of A_n and B_n decreases with increasing order (n) and apart from the $n = 3$ harmonic, odd-ordered Fourier harmonic coefficients ($n = 5, 7, 9$, etc.) appear to provide almost no refinement in an isophote's shape; therefore, beyond $n = 3$ we calculate only even harmonic coefficients, up to a maximum of $n = 10$ and still obtain a very good light profile and galaxy model. For the light profile along the major axis ($\psi = 0$), the value of sine terms are zero, hence we correct the major-axis intensity values only for the cosine perturbations (B_n).

The original ELLIPSE task is limited to only work well for face-on galaxies with almost purely elliptical isophotes (with few or no additional components), as it does not properly utilize the higher-order harmonics to fit and quantify irregularities in the isophotal shapes. Figure 2 provides a comparison of models obtained for NGC 4762 using the ELLIPSE and ISOFIT tasks.

Various isophotal parameters (ϵ, PA, A_n, and B_n) obtained from the ISOFIT task are sufficient to generate an excellent 2D model of a galaxy using the CMODEL task. The galaxy model can be further subtracted from the galaxy image to obtain a residual image, which is useful to study various foreground and background sources overlapping with the galaxy pixels. The quality of the residual image depends on how accurately the isophotal model emulates the galaxy. The quality of the model generated using the ISOFIT and CMODEL tasks can be appreciated in Figure 2.

It is evident in Figure 2 that the ELLIPSE task could not construct a very good fit to the irregular isophotes of NGC 4762 due to the high inclination of the galaxy and its (peanut shell)-shaped bulge associated with the bar (as evident in the light profile; see Figure 3). The ELLIPSE task fails to properly model the galaxy light along the disk, leaving behind bright stripes in the residual image.

3.2. Disassembling the Galaxy Image

The isophotal table obtained from ISOFIT is used by the software PROFILER (Ciambur 2016) to plot and fit the 1D radial surface brightness profile of a galaxy with respect to both its semimajor axis radius (R_{maj}) and the equivalent axis (R_{eq}). Here, R_{eq} is the geometric mean of R_{maj} and R_{min}. It is the radius of an imaginary circular isophote equivalent in area to the elliptical isophote with major- and minor-axis radius R_{maj} and R_{min}, conserving the total surface brightness of the elliptical isophote. This gives $R_{eq} = \sqrt{R_{maj}R_{min}} = R_{maj}\sqrt{1 - \epsilon}$, where ϵ is the ellipticity of the isophote. Along with the surface brightness profile, PROFILER also plots the radial profiles of the isophote's ellipticity, PA, and some of the higher-order Fourier harmonic coefficients ($B4$, $B6$, $B8$).

To decompose the galaxy light into its components, we use a wide variety of parametric analytical functions available in PROFILER. For example, Sérsic (1963) and Core-Sérsic (Graham et al. 2003) functions for galactic bulges; exponential, truncated/antitruncated exponential, and inclined-disk models for various types and orientations of disks; Ferrers (1877)

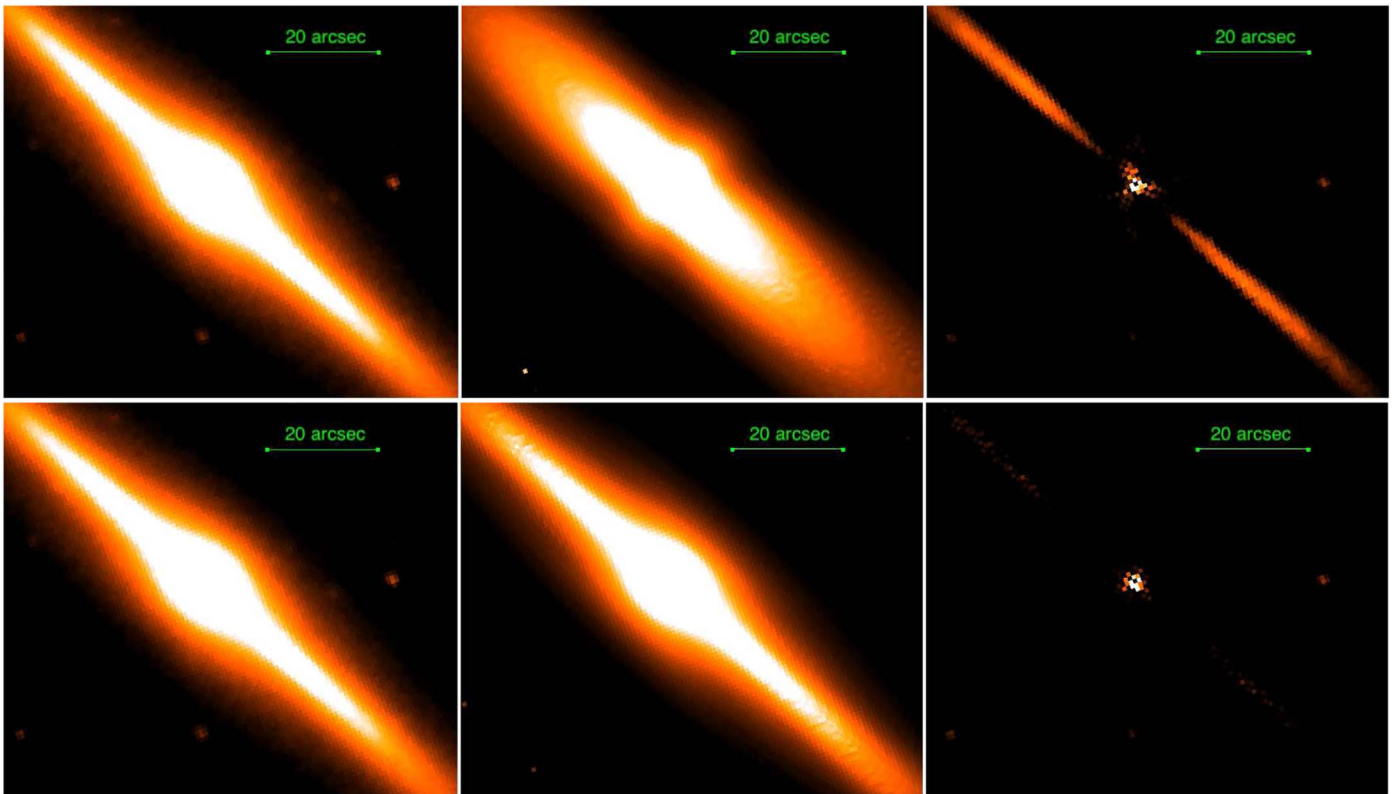[9] A curve that connects the points of equal brightness.

Figure 2. Comparison of models and residual images for NGC 4762. The first row consists of the galaxy image, model, and the residual image generated using the Ellipse and Bmodel tasks in IRAF. The second row consists of the galaxy image, model, and the residual image generated using the Isofit and Cmodel tasks (Ciambur 2015).

function for bars; Sérsic for bar-lenses/pseudobulges, Gaussian for rings, and ansae (centered at the ring/ansae radius); and PSFs for nuclear point sources. Table 2 presents the mathematical formulae for the radial surface brightness profiles of these functions, as well as the corresponding expressions to determine the apparent magnitudes from the fit parameters. More details about the surface brightness profiles of the various fitting functions can be found in Section 3 of Ciambur (2016).

We disassemble the galaxy light into its components by fitting various features present in the galaxy light profile, using the functions mentioned in Table 2. To help identify the components that are present in a galaxy, we visually inspect the galaxy image at various contrast levels using DS9; we also inspect various features present in the ellipticity, PA, $B4$, and $B6$ profiles (if required), which are beneficial in discerning galaxy components. Apart from that, we went through the literature, reviewing previous structural and kinematical studies of our galaxies, which gave us clues about the components present, their relative intensity (or surface brightness) levels, and their radial extents (sizes). In order to distinguish the components—such as an inner disk, inner ring, or nuclear star cluster—and most importantly, to identify the deficit of light at the center of a galaxy (core-Sérsic), we consulted previous works with highly resolved *HST* images (e.g., Dullo & Graham 2014).

Having obtained a fit for the light profile based on real physical structure/components for the major axis, we map it to the equivalent axis (R_{eq}), ensuring that the central ($R = 0$) surface brightness of each component remains roughly constant. The equivalent-axis parameters for each component of a galaxy are required so that PROFILER can use the circular symmetry of the equivalent axis to integrate the surface

brightness profiles and calculate the apparent magnitudes for all the components and the whole galaxy itself.

Figure 3 shows the multicomponent fit to the surface brightness profile of NGC 4762 for both the major and equivalent axes. NGC 4762 is a barred-lenticular galaxy with a small bulge, an (oval-shaped) bar-lens, a bar, an ansae, and a truncated disk. Laurikainen et al. (2005, 2007, 2011) observed that many S0 galaxies contain bars and "ovals" (also known as "lenses" or "bar-lenses"), with the inner regions of vertically heated bars appearing as boxy/(peanut-shell)-shaped structures referred to by some as "pseudobulges" (see Combes & Sanders 1981; Athanassoula 2002, 2005). The bumps in the light profile of NGC 4762, as well as the ellipticity, B_4, and B_6 profiles at $R_{maj} \approx 30''$ and $R_{maj} \approx 80''$ correspond to the perturbation of the isophotes due to the bar-lens/pseudobulge and the bar, respectively. As shown in the simulations by Saha et al. (2018) (their Figure 7), the adjacent bump ($R_{maj} \approx 80''$) and dip ($R_{maj} \approx 120''$) in the B_6 profile suggest the presence of an ansae at $R_{maj} \approx 100''$, at the end of the bar.

We also note that the decomposition results from Saha et al. (2018) (e.g., their Figure 11; see also NGC 4026 and NGC 4371 in our online figure set) support the truncated disk model[10] in NGC 4762. Furthermore, according to Kormendy & Bender (2012), the warped disk at the outer edge could be due to some ongoing tidal encounter. Table 3 lists the fit parameters for the components in NGC 4762. Light profile fits for all other galaxies can be found in the online figure set where we provide the major-axis and equivalent-axis (i.e. geometric mean axis $= \sqrt{R_{maj} R_{min}}$) surface brightness profiles (in AB magnitude

---

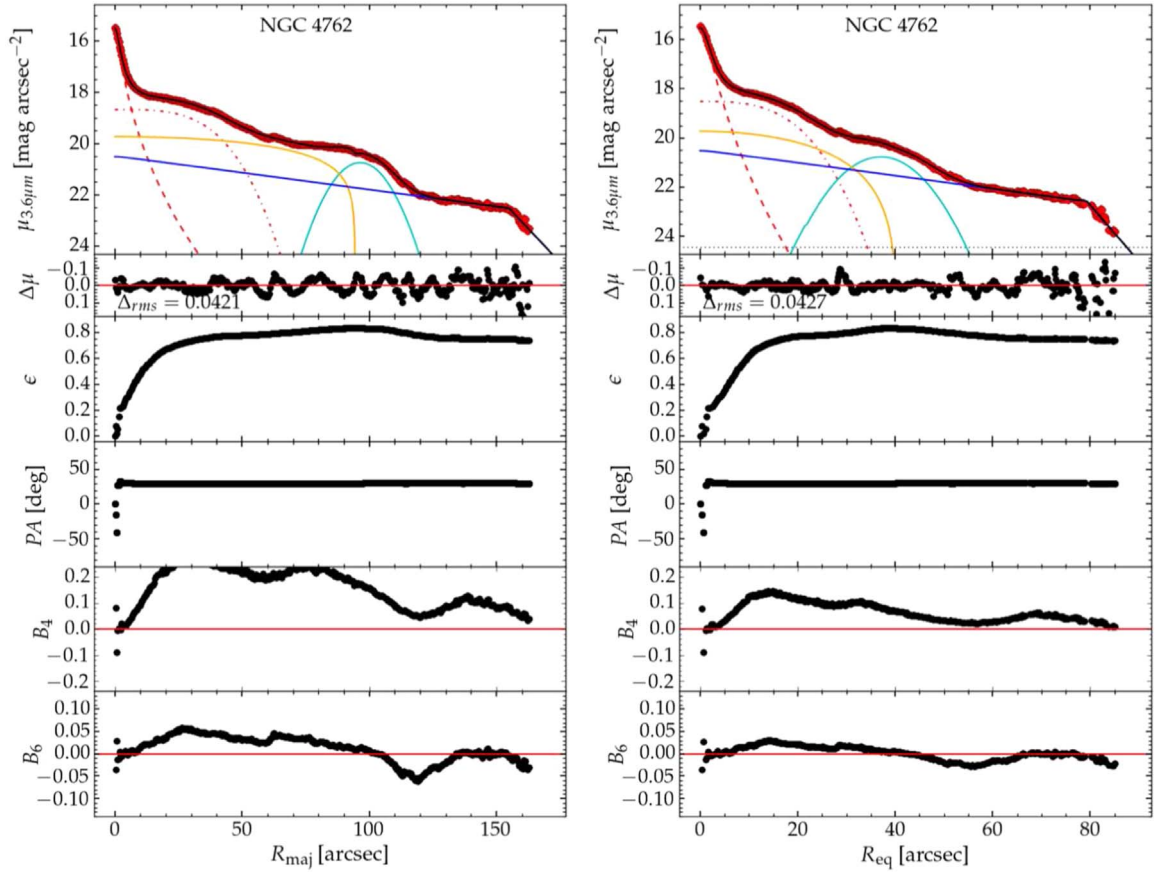[10] A truncated disk model has a change in slope beyond the truncation radius.

Figure 3. The 3.6 μm surface brightness profile of NGC 4762, plotted and fit using PROFILER. The left panel shows the profile along the major axis with $\Delta_{rms} = 0.0421$ mag arcsec^{-2}, and the right panel shows the profile along the equivalent axis with $\Delta_{rms} = 0.0427$ mag arcsec^{-2}. Physical sizes can be derived using a scale of 11 pc/$''$ based on a distance of 22.6 Mpc. NGC 4762 is a barred lenticular galaxy with its multicomponent fit comprised of a Sérsic function for the bulge (- - -), a low-index Sérsic function for the bar-lens/pseudobulge ($-\cdot-\cdot-$), a Ferrers function for the bar (——), a Gaussian for the ansae (——), and a truncated exponential model for the extended warped disk (——).

(The complete figure set (41 images) is available.)

system) for the remaining 41 ETGs that we modeled. Light profiles shown in Figures 3.1 to 3.32 are based on 3.6 μm images, Figures 3.33 to 3.38 are based on 2MASS K_s-band images, and Figures 3.39 to 3.41 are based on SDSS r'-band images. Magnitudes and stellar masses of these galaxies and their spheroids are presented in Table 4. The current paper does not directly use all the parameters from our decomposition of these light profiles; however, we intend to use them in an upcoming work, wherein will tabulate them.

3.3. Stellar Mass Calculation

We calculate the absolute magnitudes for all the galaxies, as well as their spheroids, using their apparent magnitudes (measured using PROFILER) and the distances in Table 4. These absolute magnitudes, after applying the small corrective term for cosmological dimming[11] (Tolman 1930), are used to calculate the corresponding intrinsic luminosities. The intrinsic luminosity is derived in terms of the solar luminosity in each band (see Table 1), and these luminosity values are then

converted into stellar masses by multiplying them by the stellar mass-to-light ratio (Υ_*) for each band.

Stellar mass-to-light ratios depend on many factors, such as the Initial Mass Function (IMF) of stars in a galaxy, star formation history, metallicity, and age; they can also be biased due to attenuation from dust in a galaxy. The interdependence of these factors and their effect on the stellar mass-to-light ratio is not yet understood very well. Therefore, the mass-to-light ratio dependence on these properties has large uncertainties associated with it. Meidt et al. (2014) suggest a constant, optimal, stellar mass-to-light ratio of $\Upsilon_* = 0.6$ for the 3.6 μm band, based on the Chabrier (2003) IMF, which is consistent with the age–metallicity relation and can be used for both old, metal-rich and young, metal-poor stellar populations. The emission at 3.6 and 2.2 μm is largely unaffected by the luminosity bias due to young stars, and also it undergoes minimal dust extinction (Querejeta et al. 2015), granting us a somewhat stable mass-to-light ratio. Using $\Upsilon_*^{3.6\,\mu m} = 0.6$ in the following equation from Oh et al. (2008),

$$\Upsilon_*^{3.6\,\mu m} = 0.92 \times \Upsilon_*^{K_s} - 0.05, \qquad (3)$$

which relates the stellar mass-to-light ratio at 3.6 μm to that of the K_s-band, we obtained a constant stellar mass-to-light ratio of $\Upsilon_*^{K_s} = 0.7$ for the K_s-band images. The latest relation, $\Upsilon_*^{3.6\,\mu m} = 1.03 \times \Upsilon_*^{K_s} - 0.16$ (J. Schombert 2019, private

---

[11] A magnitude of $10 \log(1 + z)$ is subtracted to account for the dimming of the observed magnitudes due to the expansion of the universe, where z is the redshift based on the galaxy distance. Redshift was calculated assuming the latest cosmological parameters $H_0 = 67.4$, $\Omega_m = 0.315$, and $\Omega_{vacuum} = 0.685$ (Planck Collaboration et al. 2018).

8

Table 2
Fitting Functions

Function	Radial Surface Brightness,[a] $\mu(R)$ (mag arcsec^{-2})	Apparent Magnitude,[b] m (mag)	Profile Parameters
Sérsic[c]	$\mu_e + (2.5 * b_n/\ln 10)[(R/R_e)^{1/n} - 1]$	$\mu_e - 5\log R_e - 2.5\log[2\pi n(\exp b_n/(b_n)^{2n})\Gamma(2n)]$	μ_e, n, R_e
Core-Sérsic[d]	$\mu' - 2.5\gamma/\alpha\log[1 + (R_b/R)^{\alpha}] + 2.5/\ln(10)[b_n((R^{\alpha} + R_b^{\alpha})/R_e^{\alpha})^{1/n\alpha}]$	$\mu_b - 2.5\log 2\pi[R_b^2/2 - \gamma + ne^{(b_n(R_b/R_e)^{1/n})}(\Gamma(2n) - \gamma(2n, (R_b/R_e)^{1/n}))]$	$\mu', R_b, R_e, n, \alpha, \gamma$
Exponential[e]	$\mu_0 + (2.5/\ln(10))(R/h)$	$\mu_0 - 2.5\log[2\pi h^2]$	μ_0, h
Truncated disk[f]	$\mu_0 + (2.5/\ln(10))(R/h_1)$ (for $R \leqslant R_b$) $\mu_b + (2.5/\ln(10))((R - R_b)/h_2)$ (for $R > R_b$)	$\mu_0 - 2.5\log 2\pi[h_1^2 + e^{-R_b/h_1}(h_2 - h_1)(h_2 + h_1 + R_b)]$	μ_0, h_1, h_2, R_b
Inclined disk[g]	$\mu_0 - 2.5\log[(R/h_r)K_1(R/h_r)]$	Integrated Numerically	μ_0, h_r
Ferrer[h]	$\mu_0 - 2.5\alpha\log[1 - (R/R_{\rm out})^{2-\beta}]$	$\mu_0 - 2.5\log[\pi R_{\rm out}^2 * {\rm hyp2F1}(-\alpha, 2/(2 - \beta), (4 - \beta)/(2 - \beta), 1)]$	$\mu_0, R_{\rm out}, \alpha, \beta$
Gaussian[i]	$\mu_r + (2.5/\ln(10))((R - R_r)^2/2\sigma^2)$	$\mu_r - 2.5\log 2\pi[\sigma^2 e^{-R_r^2/2\sigma^2} + \sigma R_r\sqrt{\pi/2}(1 + {\rm erf}(R_r/\sigma\sqrt{2}))]$	μ_r, R_r, σ

Notes.

[a] The radial surface brightness profile was obtained from the intensity profile, using $\mu(R) = -2.5\log(I(R)) +$ zero-point (see Table 1).

[b] $m = -2.5\log(L)$, where luminosity $(L) = \int 2\pi R\, I(R) dR$; $I(R)$ is the radial intensity profile.

[c] From Ciotti (1991) and Graham & Driver (2005). The quantity b_n is calculated by solving $\Gamma(2n) = 2\gamma(2n, b_n)$.

[d] Equation (5) from Graham et al. (2003); μ' and μ_b are related through Equation (6) from Graham et al. (2003). The expression for the apparent magnitude is deduced under the approximation $\alpha \to \infty$ (Equation (A20) from Trujillo et al. (2004)).

[e] Equation (14) from Graham & Driver (2005), for $n = 1$.

[f] Equation (10) from Ciambur (2016).

[g] Equation (12) from Ciambur (2016) along the major axis; $K_1(R/h_r)$ is the modified Bessel function of the second kind.

[h] From Ferrers (1877); hyp2F1 in the apparent magnitude expression represents the hypergeometric function.

[i] The parameter μ_r is the peak value of the Gaussian surface brightness profile at the "peak radius" r, and σ is the width of the Gaussian.

Table 3
Model Parameters for the NGC 4762 Light Profile

Component	Function	Major-axis Parameters	Equivalent-axis Parameters
Bulge	Sérsic	$\mu_e = 17.89$, $n = 2.36$, $R_e = 4.39$	$\mu_e = 17.09$, $n = 1.85$, $R_e = 2.24$
Bar-lens	Sérsic	$\mu_e = 18.98$, $n = 0.28$, $R_e = 28.81$	$\mu_e = 18.89$, $n = 0.31$, $R_e = 14.4$
Bar	Ferrers	$\mu_0 = 19.72$, $R_{out} = 94.56$, $\alpha = 1.65$, $\beta = 0.01$	$\mu_0 = 19.72$, $R_{out} = 40.66$, $\alpha = 3.81$, $\beta = 0.01$
Ansae	Gaussian	$\mu_r = 20.74$, $R_r = 96.45$, FWHM $= 21.30$	$\mu_r = 20.77$, $R_r = 37.06$, FWHM $= 15.89$
Disk	Truncated Exponential	$\mu_0 = 20.48$, $R_b = 155.07$, $h1 = 82.62$, $h2 = 10.23$	$\mu_0 = 20.48$, $R_b = 79.36$, $h1 = 40.92$, $h2 = 4.72$

Note. Scale size parameters (R_e, R_{out}, R_r, $h1$, and $h2$) are in units of arcseconds, and surface brightnesses (μ_e, μ_0, and μ_r) pertains to the 3.6 μm band (AB mag). FWHM of the Gaussian can be related to its standard deviation (σ) by FWHM $= 2\sigma\sqrt{2\ln 2}$. The equivalent axis is also known as the "geometric mean" axis, given by the square root of the product of the major and minor axes.

communication), which is based on a larger $K_s - 3.6\,\mu$m data set, also revealed a consistent value for $\Upsilon_*^{K_s}$.

For our three r'-band data, we used an average stellar mass-to-light ratio of $\Upsilon_*^{r'} \equiv M_*/L_{r'} = 2.8$ to obtain the corresponding stellar masses. We calibrated $\Upsilon_*^{r'}$ using

$$\frac{M_*}{L_{r'}} = \left(\frac{L_{K_s}}{L_{r'}}\right)\left(\frac{M_*}{L_{K_s}}\right), \qquad (4)$$

ensuring that the galaxy stellar masses are consistent with the masses obtained using K_s-band magnitudes (obtained from 2MASS imaging of these galaxies), and a stellar mass-to-light ratio of $\Upsilon_*^{K_s} = 0.7$. We present the spheroid and total galaxy stellar masses for our galaxies in Table 4.

3.4. Comparison of Stellar Masses

Here, we compare the galaxy stellar masses measured using the 3.6 μm band images (calculated as described above) with the galaxy stellar masses calculated using (already available) K_s, i', and r'-band magnitudes and three different formulae for the corresponding stellar mass-to-light ratios. The comparison and the best-fit lines are shown in Figure 4, where the horizontal axis designates the 3.6 μm band-derived masses, labeled $\log(M_{*,\mathrm{Gal}_{3.6\,\mu m}}/M_\odot)$, and the vertical axis depicts the masses based on the K_s, i', and r' band magnitudes, labeled $\log(M_{*,\mathrm{Gal}_{K_s,i',r'}}/M_\odot)$.

The black dots in Figure 4 show the masses of 71 galaxies, calculated here using K_s-band magnitudes and ($B - K_s$ color-dependent) K_s-band stellar mass-to-light ratios from Table 1 of Bell & de Jong (2001), placed with respect to our (3.6 μm band) stellar masses. The K_s and B-band magnitudes were obtained from the 2MASS catalog (Jarrett et al. 2003) and the Third Reference Catalogue (RC3) of Bright Galaxies (de Vaucouleurs et al. 1991), respectively. The K_s-band magnitudes obtained from the 2MASS data reduction pipelines are usually underestimated (Schombert & Smith 2012). We used Equation (1) from Scott et al. (2013) to correct for the underestimation; the size of this correction was <0.35 mag. The K_s-band stellar mass-to-light ratios were brought to a Chabrier IMF, from the scaled/diet Salpeter IMF used by Bell & de Jong (2001), by subtracting an IMF-dependent constant of 0.093 dex (Taylor et al. 2011; Mitchell et al. 2013). In Figure 5, we also present the $B - K_s$ color versus the K_s-band magnitude for our sample, which is consistent with the color–magnitude diagram presented by Graham & Soria (2019, their Figure 11), implying that our galaxies belong to the red sequence, which flattens ($B - K_s \approx 4$) at bright magnitudes (MAG$_{K_s}$ < −22 mag).

The red triangles in Figure 4 are the masses of 23 galaxies calculated using i'-band magnitudes and ($g' - i'$ color-dependent)

i'-band stellar mass-to-light ratios (based on a Chabrier IMF) from Taylor et al. (2011), their Equation (7)).

The blue squares represent the masses of 23 galaxies calculated using r'-band magnitudes and ($g' - r'$ color-dependent) r'-band stellar mass-to-light ratios from Roediger & Courteau (2015), which are based on the Stellar Population Synthesis (SPS) model by Conroy et al. (2009). The apparent galaxy magnitudes in the SDSS g', r', and i'-bands were collected from the NASA/IPAC Extragalactic Database.

The black, blue, and red lines in Figure 4 represent the least-squares fits to the three corresponding types of data points. We found that there is almost a linear one-to-one relationship between the masses derived from the K_s-band (black line) and our 3.6 μm-derived masses. The galaxy stellar masses based on r'- and i'-band magnitudes (blue line and red line, respectively) are systematically offset. Although the offset is small, it systematically increases at higher galaxy masses. Such an offset has been noticed in a few other studies (e.g., Taylor et al. 2011; Graham et al. 2019). The systematic offset between the above three lines can be attributed mainly to the IMFs, the star formation rates, and the stellar evolutionary histories assumed to derive the mass-to-light ratios. Various telescope pipeline processes may also introduce some systematic uncertainties in the apparent magnitudes.

Figure 4 mainly serves to illustrate that the use of different stellar mass-to-light ratio prescriptions for luminosities (magnitudes) obtained in different bands can produce different stellar masses for a galaxy and its components (see Kannappan & Gawiser (2007) for a detailed comparison of masses calculated using different methods). In passing, we note that we will explore whether this may be a factor contributing to the offset observed by Shankar et al. (2016) between galaxies with directly measured black hole masses and the population at large.

Differences in estimated stellar mass will lead to different estimates of a galaxy's black hole mass when using the black hole mass scaling relations presented here and elsewhere. Hence, in our forthcoming equations for the M_{BH}–$M_{*,\mathrm{sph}}$ and M_{BH}–$M_{*,\mathrm{gal}}$ relations, we are including a conversion or correcting coefficient, υ (lower case upsilon), for the stellar masses (see Davis et al. 2019). This stellar mass correction coefficient accounts for the difference in stellar mass of a galaxy due to either the difference in the stellar mass-to-light ratio (Υ_*) used for the same passband, or to a different passband magnitude as well as a different mass-to-light ratio applied to it. If $\Upsilon_*^{\mathrm{IRAC1}}$ is the user-preferred *Spitzer* 3.6 μm band stellar mass-to-light ratio, the correction coefficient $\upsilon_{*,\mathrm{IRAC1}}$ is given by

$$\upsilon_{*,\mathrm{IRAC1}} = \frac{\Upsilon_*^{\mathrm{IRAC1}}}{0.6}, \qquad (5)$$

Table 4
Galaxy Sample

Galaxy	Type	Core	Distance (Mpc)	$\log(M_{BH}/M_\odot)$	MAG_{sph} (mag)	MAG_{gal} (mag)	$\log(M_{*,sph}/M_\odot)$	$\log(M_{*,gal}/M_\odot)$
(1)	(2)	(3)	(4)	(5)	(6)	(7)	(8)	(9)
A1836 BCG[a]	E1-2	yes	158.00 ± 11.06	9.59 ± 0.06[5a, G]	-24.56 ± 0.20	-24.56 ± 0.20	11.70 ± 0.12	11.70 ± 0.12
A3565 BCG	E1	no	40.70 ± 2.90[4a]	9.04 ± 0.09[5a, G]	-23.22 ± 0.6	-23.26 ± 0.20	11.47 ± 0.26	11.49 ± 0.12
NGC 0307[b]	SAB0	no	52.80 ± 3.70	8.34 ± 0.13[5c, S]	-20.31 ± 0.80	-21.14 ± 0.20	10.43 ± 0.33	10.76 ± 0.12
NGC 0404	S0	no	3.06 ± 0.37	4.85 ± 0.13[5d, S]	-14.43 ± 0.60	-17.33 ± 0.20	7.96 ± 0.27	9.12 ± 0.12
NGC 0524	SA0(rs)	yes	23.30 ± 1.63	8.92 ± 0.10[5e, S]	-20.97 ± 0.60	-22.21 ± 0.20	10.57 ± 0.26	11.07 ± 0.12
NGC 1194	S0	no	53.20 ± 3.70	7.81 ± 0.04[5f, M]	-21.31 ± 0.80	-21.87 ± 0.20	10.71 ± 0.33	10.94 ± 0.12
NGC 1275	E	no	72.9 ± 5.10[4a]	8.90 ± 0.20[5g, G]	-24.14 ± 0.60	-24.23 ± 0.20	11.84 ± 0.26	11.88 ± 0.12
NGC 1374	S0	no?	19.20 ± 1.34	8.76 ± 0.05[5h, S]	-20.09 ± 0.60	-20.83 ± 0.20	10.22 ± 0.26	10.52 ± 0.12
NGC 1407	E	yes	28.05 ± 3.37	9.65 ± 0.08[5h, S]	-23.19 ± 0.60	-23.34 ± 0.02	11.46 ± 0.27	11.52 ± 0.12
NGC 1550[a]	E1	yes	51.57 ± 3.61	9.57 ± 0.06[5h, S]	-23.14 ± 0.20	-23.14 ± 0.20	11.13 ± 0.12	11.13 ± 0.12
NGC 1600	E3	yes	64.00 ± 4.48	10.23 ± 0.05[5i, S]	-24.09 ± 0.20	-24.09 ± 0.20	11.82 ± 0.12	11.82 ± 0.12
NGC 2787	SB0(r)	no	7.30 ± 0.51	7.60 ± 0.06[5j, G]	-17.35 ± 0.60	-19.51 ± 0.20	9.13 ± 0.26	9.99 ± 0.12
NGC 3665	S0	no	34.70 ± 2.43	8.76 ± 0.10[5k, G]	-22.12 ± 0.60	-22.74 ± 0.20	11.03 ± 0.26	11.28 ± 0.12
NGC 3923	E4	yes	20.88 ± 2.70	9.45 ± 0.13[5l, S]	-23.02 ± 0.20	-23.02 ± 0.20	11.40 ± 0.15	11.40 ± 0.12
NGC 4026	SB0	no	13.20 ± 0.92	8.26 ± 0.11[5m, S]	-19.82 ± 0.80	-20.44 ± 0.20	10.11 ± 0.33	10.36 ± 0.12
NGC 4339	S0	no	16.00 ± 1.33	7.63 ± 0.33[5n, S]	-18.72 ± 0.60	-19.96 ± 0.20	9.67 ± 0.26	10.17 ± 0.12
NGC 4342	ES/S0	no	23.00 ± 1.00	8.65 ± 0.18[5o, S]	-19.38 ± 0.60	-20.20 ± 0.20	9.94 ± 0.25	10.26 ± 0.12
NGC 4350	EBS	no	16.80 ± 1.18	8.86 ± 0.41[5p, SG]	-20.22 ± 0.60	-20.90 ± 0.20	10.28 ± 0.26	10.55 ± 0.12
NGC 4371	SB(r)0	no	16.90 ± 1.48	6.84 ± 0.08[5l, S]	-19.27 ± 0.60	-21.03 ± 0.20	9.89 ± 0.26	10.60 ± 0.12
NGC 4429	SB(r)0	no	16.50 ± 1.60	8.18 ± 0.09[5q, G]	-20.69 ± 0.60	-21.79 ± 0.20	10.46 ± 0.26	10.90 ± 0.12
NGC 4434	S0	no	22.40 ± 1.57	7.84 ± 0.17[5n, S]	-19.32 ± 0.60	-20.00 ± 0.20	9.91 ± 0.26	10.18 ± 0.12
NGC 4486B[b]	E1	no	15.30 ± 0.32	8.76 ± 0.24[5r, S]	-17.90 ± 0.80	-17.90 ± 0.20	9.46 ± 0.33	9.46 ± 0.12
NGC 4526	S0	no	16.90 ± 1.69	8.67 ± 0.04[5s, G]	-21.27 ± 0.60	-22.14 ± 0.20	10.70 ± 0.26	11.04 ± 0.12
NGC 4552	E	no	14.90 ± 0.95	8.67 ± 0.05[5t, S]	-21.75 ± 0.60	-21.92 ± 0.20	10.88 ± 0.25	10.95 ± 0.12
NGC 4578	S0(r)	no	16.30 ± 1.14	7.28 ± 0.35[5n, S]	-18.97 ± 0.60	-20.10 ± 0.20	9.77 ± 0.26	10.23 ± 0.12
NGC 4649	E2	yes	16.40 ± 1.10	9.67 ± 0.10[5u, S]	-23.14 ± 0.20	-23.14 ± 0.20	11.44 ± 0.12	11.44 ± 0.12
NGC 4742	S0	no	15.50 ± 1.15	7.15 ± 0.18[5v, S]	-19.21 ± 0.60	-19.92 ± 0.20	9.87 ± 0.26	10.15 ± 0.12
NGC 4751[a]	S0	yes?	26.92 ± 1.88	9.15 ± 0.05[5h, S]	-21.53 ± 0.60	-22.11 ± 0.20	10.49 ± 0.26	10.72 ± 0.12
NGC 4762	SB0	no	22.60 ± 3.39	7.36 ± 0.15[5n, S]	-19.45 ± 0.60	-22.19 ± 0.20	9.97 ± 0.28	11.06 ± 0.12
NGC 5018	S0	no	40.55 ± 4.87	8.02 ± 0.09[5l, S]	-21.97 ± 0.60	-22.91 ± 0.20	10.98 ± 0.27	11.35 ± 0.12
NGC 5252	S0	no	96.80 ± 6.78	9.00 ± 0.40[5w, G]	-21.67 ± 0.60	-23.00 ± 0.20	10.85 ± 0.26	11.38 ± 0.12
NGC 5328[a]	E1	yes	64.10 ± 4.49	9.67 ± 0.15[5h, S]	-24.03 ± 0.20	-24.03 ± 0.20	11.49 ± 0.12	11.49 ± 0.12
NGC 5419	E2-3	yes	56.20 ± 3.93	9.86 ± 0.14[5x, S]	-23.15 ± 0.20	-23.15 ± 0.20	11.44 ± 0.12	11.44 ± 0.12
NGC 5516[a]	E1-2	yes?	58.44 ± 4.09	9.52 ± 0.06[5h, S]	-23.91 ± 0.20	-23.91 ± 0.20	11.44 ± 0.12	11.44 ± 0.12
NGC 5813	S0	yes	31.30 ± 2.60	8.83 ± 0.06[5y, S]	-21.68 ± 0.60	-22.62 ± 0.20	10.86 ± 0.26	11.23 ± 0.12
NGC 5845	ES	no	25.20 ± 1.76	8.41 ± 0.22[5z, S]	-19.83 ± 0.60	-20.32 ± 0.20	10.12 ± 0.26	10.32 ± 0.12
NGC 6086[b]	E	yes	138.00 ± 9.66	9.57 ± 0.16[5aa, S]	-23.03 ± 0.60	-23.03 ± 0.20	11.52 ± 0.26	11.52 ± 0.12
NGC 6861	ES	no	27.30 ± 4.49	9.30 ± 0.08[5h, S]	-21.88 ± 0.60	-22.10 ± 0.20	10.94 ± 0.29	11.02 ± 0.12
NGC 7052	E4	yes	66.40 ± 4.65[4a]	8.57 ± 0.23[5ab, G]	-23.19 ± 0.20	-23.19 ± 0.20	11.46 ± 0.12	11.46 ± 0.12
NGC 7332	SB0(pec)	no	24.89 ± 2.49	7.11 ± 0.20[5ac, S]	-20.08 ± 0.80	-21.63 ± 0.20	10.22 ± 0.34	10.84 ± 0.12
NGC 7457	S0	no	14.00 ± 0.98	7.00 ± 0.30[5ad, S]	-18.04 ± 0.60	-20.00 ± 0.20	9.40 ± 0.26	10.19 ± 0.12

Notes. Columns: (1) Galaxy name. (2) Morphology, based on our decompositions. (3) Presence of partially depleted core. (4) Distance, primarily from the corresponding paper presenting the measured SMBH mass (M_{BH}). For some galaxies that did not have any error associated with these, we assigned an error of 7% (see Section 3.5). (5) Directly measured supermassive black hole mass, reference, and method used (S: Stellar dynamics, G: Gas dynamics, M: H$_2$O Megamaser). The error in M_{BH}, obtained from the corresponding papers, was added in quadrature with the distance error. (6) Spheroid absolute magnitude at 3.6 μm, unless otherwise noted in Column 1 (AB mag system). (7) Total galaxy absolute magnitude at 3.6 μm, unless otherwise noted in Column 1 (AB mag system). (8) Spheroidal mass measured in this work; see Section 3.3. (9) Galaxy mass measured in this work.
[a] 2MASS K_s-band galaxy images.
[b] SDSS r'-band galaxy images.

References. 4a = NED (Virgo + GA + Shapley)-corrected Hubble flow distances; 5a = Dalla Bontà et al. (2009); 5b = Walsh et al. (2017); 5c = Erwin et al. (2018); 5d = Nguyen et al. (2017); 5e = Krajnović et al. (2009); 5f = Kuo et al. (2011); 5g = Scharwächter et al. (2013); 5h = Rusli et al. (2013b); 5i = Thomas et al. (2016); 5j = Sarzi et al. (2001); 5k = Onishi et al. (2017); 5l = Saglia et al. (2016); 5m = Gültekin et al. (2009b); 5n = Krajnović et al. (2018); 5o = Cretton & van den Bosch (1999); 5p = Pignatelli et al. (2001); 5q = Davis et al. (2018b); 5r = Kormendy et al. (1996); 5s = Gould (2013); 5t = Hu (2008); 5u = Shen & Gebhardt (2010); 5v = Tremaine et al. (2002); 5w = Capetti et al. (2005); 5x = Mazzalay et al. (2016); 5y = Hu (2008); 5z = Gebhardt et al. (2003); 5aa = McConnell et al. (2011); 5ab = van der Marel & van den Bosch (1998); 5ac = Batcheldor et al. (2013); 5ad = Schulze & Gebhardt (2011).

where 0.6 is the stellar mass-to-light ratio for the IRAC1 (3.6 μm) passband used in this work, adopted from Meidt et al. (2014).

The correcting coefficient (υ), for the masses (M_{*,K_s}, $M_{*,r'}$, $M_{*,i'}$) derived using the K_s-, i'-, and r'-band magnitudes with the three stellar mass-to-light ratio trends shown in Figure 4,
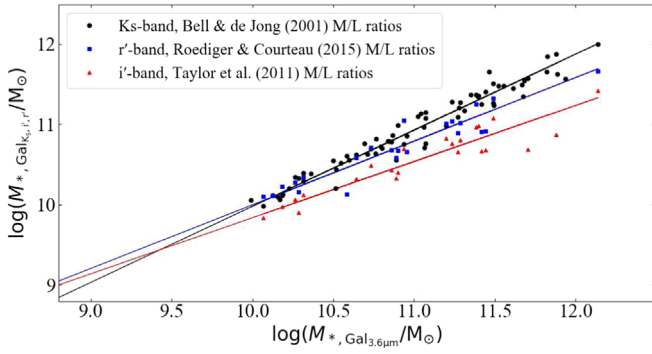
Figure 4. Comparison of the galaxy stellar masses for our sample. The masses on the horizontal axis are calculated from 3.6 μm imaging with $\Upsilon_*^{3.6\,\mu m} = 0.6$, while the masses derived from the K_s-, r'-, and i'-bands are shown on the vertical axis. The black dots represent the total galaxy stellar masses of 71 galaxies based on improved K_s-band magnitudes and ($B - K_s$ color-dependent) K_s-band stellar mass-to-light ratios from Bell & de Jong (2001). Blue squares show the total galaxy stellar masses of 23 galaxies obtained using r'-band magnitudes and $g' - r'$ color-dependent mass-to-light ratios from Roediger & Courteau (2015), and the red triangles mark the total galaxy stellar masses of the same 23 galaxies calculated using i'-band magnitudes and $g' - i'$ color-dependent mass-to-light ratios from Taylor et al. (2011). Black, blue, and red lines are the least-squares regression lines defining a relation between these masses.
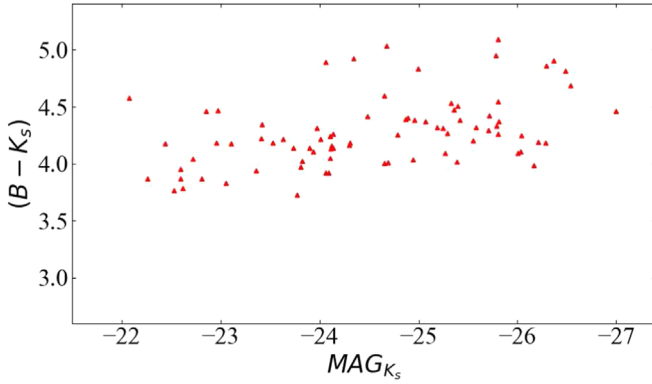
Figure 5. The $B - K_s$ color vs. K_s-band absolute magnitude (in Vega system) diagram for 82 ETGs. Most of our sample resides along the relatively flat arm (for MAG$_{K_s} < -22$ mag) of the color–magnitude diagram presented by Graham & Soria (2019).

can be expressed as follows:

$$\log \upsilon_{*,K_s} = -0.06 \log\left(\frac{M_{*,K_s}}{10^{10}M_\odot}\right) - 0.06, \quad (6)$$

$$\log \upsilon_{*,r'} = -0.26 \log\left(\frac{M_{*,r'}}{10^{10}M_\odot}\right) + 0.03, \quad (7)$$

$$\log \upsilon_{*,i'} = -0.43 \log\left(\frac{M_{*,i'}}{10^{10}M_\odot}\right) - 0.21. \quad (8)$$

These equations are obtained by calculating the offset of the three lines shown in Figure 4 from our 3.6 μm-derived galaxy masses calculated in Section 3.3. Users intending to estimate black hole masses from our scaling relations using their galaxy masses calculated based on the above three prescriptions can directly substitute the corresponding expression for υ in the M_{BH} relations.

For estimating M_{BH} using galaxy masses based on some other pass-band luminosities and mass-to-light ratios, we suggest users calculate the conversion coefficient (υ) for their masses using our Equation (5).

3.5. Error Analysis

Our spheroid and galaxy stellar masses depend on three main independent quantities: the stellar mass-to-light ratio (Υ_*), distance (D), and the apparent magnitude (m). We have estimated the error in these three quantities and added them in quadrature.

Our galaxy sample, dominated by near-infrared imaging, enables us to apply a relatively stable stellar mass-to-light ratio adopted from Meidt et al. (2014) and Querejeta et al. (2015). Meidt et al. (2014) recommend the use of a more liberal 15% uncertainty on the 3.6 μm stellar mass-to-light ratio, accounting for an atypical evolutionary history or nonstellar emissions (which are dominant in red colors). Because $\Upsilon_*^{r'}$ for our r'-band images is calibrated against 2MASS imaging and $\Upsilon_*^{K_s}$, and $\Upsilon_*^{K_s}$ in turn is derived from $\Upsilon_*^{3.6\,\mu m}$, as described in Section 3.3, we assign a constant uncertainty of 15% to the stellar mass-to-light ratios for all the galaxies.

For most of the 42 galaxies (Table 4) that we modeled, we obtained the error in their distances from the publication that presented their directly measured SMBH mass. For the rest of the galaxies (including those from Savorgnan & Graham (2016a)), we are using a constant error of 7% in their distances, which is a typical percentage error in the (Virgo + GA + Shapley)-corrected Hubble flow distances obtained from NASA/IPAC Extragalactic Database.

Imprecise sky subtraction, errors in the telescope's PSF size measurement, and errors in the decomposition of the galaxy light are all potential sources of error in the apparent magnitudes. The decomposition may contain errors for many possible reasons: neglecting a component of the galaxy, misinterpreting a component's size or position, an error in the calibrated zero-point magnitude, misinterpreting nuclear components or being unable to resolve it, etc. It is nearly impossible to quantify all these errors.

If we assume that we have used an accurate method to measure the sky level and the telescope's PSF, and trust various telescope pipelines (where we downloaded our images) for their zero-point flux calibration, then our main source of error in magnitude will be the error in the galaxy light decomposition process. Although PROFILER provides the formal random error for each fit parameter of the various components of a galaxy, which is the rms error obtained by least-squares minimization between data and the fitting function, it is very small. To better quantify the uncertainty in the decomposition, we have followed the (light profile fit quality) grading scheme described by Savorgnan & Graham (2016a) in their Section 4.2.1, except that we have assigned symmetric errors of 0.2 mag, 0.6 mag, and 0.8 mag to the spheroidal components of our grade-1, grade-2, and grade-3 galaxies, respectively.

As we are dealing with the stellar masses in log, we calculate these errors in log (dex). An error of δm mag in apparent magnitude, a δD error in distance, and a $\delta\Upsilon_*$ error in the stellar mass-to-light ratio, added in quadrature, give us the error in the stellar mass (in dex):

$$\delta \log M = \sqrt{\left(\frac{\delta m}{2.5}\right)^2 + \left(2\frac{\delta D}{D\ln(10)}\right)^2 + \left(\frac{\delta\Upsilon_*}{\Upsilon_*\ln(10)}\right)^2}. \quad (9)$$

We use the above equation to calculate the uncertainty in spheroid masses. The uncertainty in the measurement of total galaxy stellar mass should be less than the uncertainty in the spheroid mass; as for total galaxy mass we do not need to go

through the complicated multi-component decomposition process for most of the galaxies. Therefore, we assign a constant error of 0.12 dex to the galaxy masses, which is equivalent to the total quadrature error (calculated using Equation (9)) assigned to the spheroid masses of our grade-1 galaxies, which are mostly single component galaxies.

4. Results and Discussion

We performed a Bivariate Correlated Errors and Intrinsic Scatter (BCES) regression (Akritas & Bershady 1996) between the SMBH masses and both the spheroid masses and the total galaxy masses of our sample. BCES is simply an extension of the Ordinary Least Squares (OLS) estimator permitting dependent measurement errors in both the variables. We use the bisector line obtained by the BCES[12] regression; this line symmetrically bisects the regression lines obtained using BCES $(X|Y)$[13] and BCES$(Y|X)$.[14] The bisector regression line offers equal treatment to the measurement errors in both the coordinates, and allows for intrinsic scatter. In addition to the BCES routine, we also used the modified FITEXY routine (Press et al. 1992; Tremaine et al. 2002) to perform a regression on our data for the $M_{\rm BH}$–$M_{*,\rm sph}$ and $M_{\rm BH}$–$M_{*,\rm gal}$ relations. We found results highly consistent with those of the BCES regression, within the 1σ bounds.

In our analysis, we have excluded eight galaxies (Mrk 1216, NGC 404, NGC 1277, NGC 1316, NGC 2787, NGC 4342, NGC 4486B, and NGC 5128), which leaves us with a reduced data set of 76 ETGs. In all our plots hereafter, these galaxies are shown by a black star (except for Mrk 1216). We excluded Mrk 1216 from our regression analysis because we did not obtain a suitably resolved and deep image to determine the spheroidal component of this galaxy.

NGC 1316 (Fornax-A) and NGC 5128 (Cen A) are galaxy mergers in progress. According to Kormendy & Ho (2013), these two galaxies have much higher bulge masses compared to their central SMBH masses, which can make them stand out in the black hole mass scaling relations.

NGC 404 has the lowest SMBH mass in our sample. Nguyen et al. (2017) provide a measured black hole mass of $7^{+1.5}_{-2.0} \times 10^4\, M_\odot$, using Jeans Anisotropic Modeling (JAM) of stellar orbits, along with a 3σ upper limit of $1.5 \times 10^5\, M_\odot$ in $M_{\rm BH}$. Although NGC 404 does not appear to be an outlier in our data set, as it follows the regression lines at the low-mass end, we still exclude it because it would anchor the low-mass end of the relationship and we do not want our regression lines to be biased by any individual galaxy.

We also exclude NGC 4342 and NGC 4486B, because they have been tidally stripped due to the gravitational pull of their respective nearby massive companion galaxies, NGC 4365 (Blom et al. 2014) and NGC 4486 (Batcheldor et al. 2010). NGC 4342 and NGC 4486B are left with a significantly reduced galaxy mass and can be seen clearly offset in our $M_{\rm BH}$–$M_{*,\rm sph}$ and $M_{\rm BH}$–$M_{*,\rm gal}$ diagrams (toward the low-mass side of the $M_{*,\rm sph}$ and $M_{*,\rm gal}$ coordinate axes). NGC 221 (M32) is another, similar, well-known galaxy offset due to tidal stripping from the massive companion galaxy M31 (e.g.,

Graham 2002). Such compact elliptical galaxies are relatively rare among the general population and are recommended to be excluded from $M_{\rm BH}$–$M_{*,\rm gal}$ scaling relations (see Graham & Soria 2019).

NGC 1277 (peculiar morphology) and NGC 2787 are two disk galaxies that are potential outliers at the high- and low-mass ends of our relations, respectively. They have a torquing effect on our regression lines, especially for the subcategory of galaxies with a disk (ES/S0). We have therefore excluded these galaxies from our regressions, to avoid biasing the slope of our scaling relations. Furthermore, the stellar mass for NGC 1277 is measured from V-band imaging (Graham et al. 2016b) and a stellar mass-to-light ratio based on an unusually bottom-heavy IMF (Martín-Navarro et al. 2015). According to Figure 8 of Courteau et al. (2014), stellar mass-to-light ratios based on a bottom heavy IMF can be a factor of ~6 higher than stellar mass-to-light ratios based on the Chabrier IMF that we have adopted, which is likely to be the principal reason for NGC 1277 standing out at the high-mass end of our relations.

The above galaxies remain excluded in all the regressions presented in this paper. In Figures 6–11, we identify an additional five galaxies with a peculiar morphology, to investigate whether they might be outliers, but they are included in the regressions.

In our search for the underlying relation between SMBH mass and host galaxy property, we explored various possibilities for the scaling relations by dividing the galaxy sample into different categories: Sérsic and core-Sérsic galaxies; galaxies with and without disks; and galaxies with and without bars. We will analyze and discuss the scaling relations for these categories in the following sections.

4.1. Sérsic and Core-Sérsic Galaxies

Core-Sérsic galaxies are massive ETGs with central SMBHs that likely formed from the merging of the central black holes of two or more galaxies (Begelman et al. 1980; Graham 2004; Merritt 2006). They occupy the high-mass end of the black hole mass scaling relations. The discovery of the bent $M_{\rm BH}$–$L_{\rm sph}$ ($M_{*,\rm sph}$) relation for Sérsic and core-Sérsic galaxies was based on a mixed sample of elliptical, lenticular, and spiral galaxies (Graham 2012; Graham & Scott 2013; Scott et al. 2013). In our work, we investigated the nature of the above relation based on a larger sample of only ETGs.

We have categorized Sérsic and core-Sérsic galaxies based on their central light profiles, as determined from previous studies of high-resolution images (Ferrarese et al. 2006; Richings et al. 2011; Dullo & Graham 2014). Figure 6 presents two regressions performed on the two categories (Sérsic and core-Sérsic) for the SMBH mass versus both the spheroid stellar mass (left panel) and the total galaxy stellar mass (right panel) relations.

The BCES bisector regression of our 45 Sérsic and 31 core-Sérsic galaxies revealed $M_{\rm BH} \propto M_{*,\rm sph}^{1.30\pm0.14}$ and $M_{\rm BH} \propto M_{*,\rm sph}^{1.38\pm0.21}$, respectively. For the black hole mass versus total galaxy mass diagram, we obtained $M_{\rm BH} \propto M_{*,\rm gal}^{1.61\pm0.18}$ and $M_{\rm BH} \propto M_{*,\rm gal}^{1.47\pm0.18}$ for Sérsic and core-Sérsic galaxies, respectively. For both the $M_{\rm BH}$–$M_{*,\rm sph}$ and $M_{\rm BH}$–$M_{*,\rm gal}$ relations, the slopes and intercepts of the regression lines for the Sérsic (blue line) and core-Sérsic (red line) ETGs are consistent within the 1σ confidence interval. Slopes and intercepts for the BCES bisector, as well as BCES$(Y|X)$ and BCES$(X|Y)$ regression lines for the Sérsic and core-Sérsic galaxies,

---

[12] To perform the BCES regression, we used the PYTHON script (available at https://github.com/rsnemmen/BCES) written by Nemmen et al. (2012), which we modified to calculate the intrinsic scatter (Equation (1) from Graham & Driver 2007).

[13] Minimizes scatter in the X-direction.

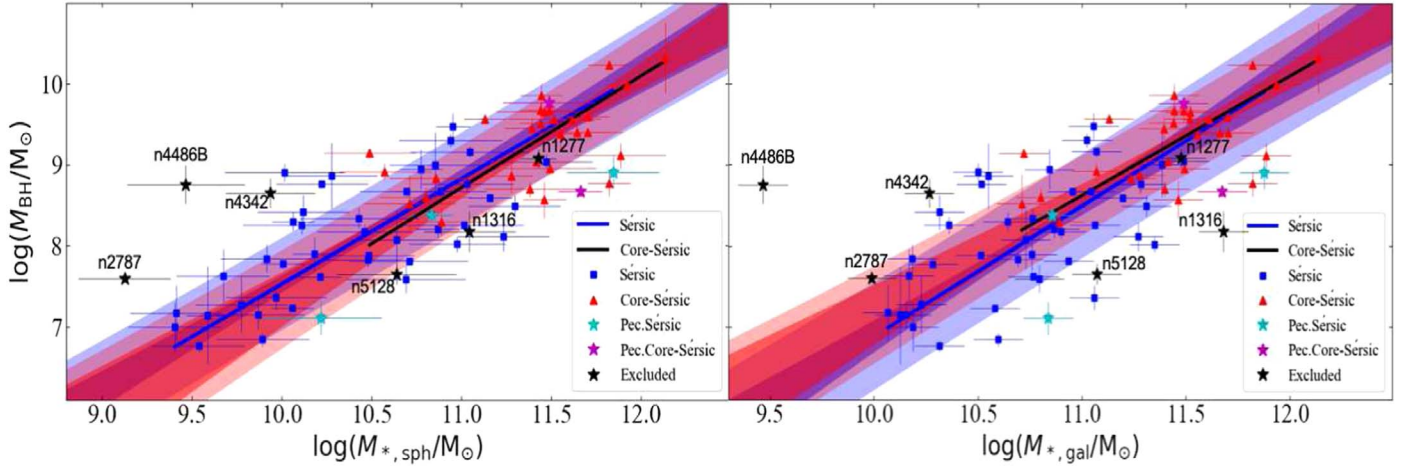[14] Minimizes scatter in the Y-direction.

Figure 6. Black hole mass vs. spheroid stellar mass (left) and total galaxy stellar mass (right). Over-plotted are Sérsic galaxies (blue squares) and core-Sérsic galaxies (red triangles). The blue and black lines represent the corresponding bisector regression lines of Sérsic and core-Sérsic galaxies, and the dark blue and dark red bands display the $\pm 1\sigma$ uncertainty on the slope and intercept of the lines. The light blue and light red regions show the $\pm 1\sigma$ rms scatter of the data about the blue and black regression lines for Sérsic and core-Sérsic galaxies, respectively. Peculiar Sérsic (three cyan stars) and core-Sérsic (two magenta stars) galaxies are depicted with different symbols, but they were included in the regressions. The six black stars are galaxies excluded from the regression: NGC 1316 and NGC 5128 are mergers; NGC 4486B and NGC 4342 are stripped galaxies; and NGC 1277 and NGC 2787 are potential outliers at the extremities of the spheroid mass range, which may bias the regression line. Their relative positions remain the same from Figures 6 to 10. We do not show the remaining two excluded galaxies: NGC 404 lies at low-mass end of the diagrams (see Figure 11), and we could not properly measure the spheroid and total galaxy stellar masses for Mrk 1216 due to the lack of a good image. It is evident that both populations overlap with each other, leading us to the conclusion that there is no "bend" in the $M_{\rm BH}$–$M_{*,\rm sph}$ or $M_{\rm BH}$–$M_{*,\rm gal}$ relations for ETGs with $M_{\rm BH} \gtrsim 10^7\,M_\odot$ due to Sérsic or core-Sérsic galaxies (see also Savorgnan et al. 2016).

for both the $M_{\rm BH}$–$M_{*,\rm sph}$ and $M_{\rm BH}$–$M_{*,\rm gal}$ relations can be found in Table 5.

Our findings are unlike the relations $M_{\rm BH} \propto M_{*,\rm sph}^{(2.22 \pm 0.58)}$ and $M_{\rm BH} \propto M_{*,\rm sph}^{(0.94 \pm 0.14)}$ obtained by Scott et al. (2013) for their Sérsic and core-Sérsic galaxies, respectively. It appears that they may have found the break in the $M_{\rm BH}$–$M_{*,\rm sph}$ relation due to the inclusion of spiral galaxies, which steepened the $M_{\rm BH}$–$M_{*,\rm sph}$ relation for for their Sérsic galaxies (see Section 4.4).

The consistency of the regression lines for the Sérsic and core-Sérsic ETGs suggests that all the ETGs (whether Sérsic or core-Sérsic) may follow single log-linear relations in the $M_{\rm BH}$–$M_{*,\rm sph}$ and $M_{\rm BH}$–$M_{*,\rm gal}$ diagrams. Fitting single BCES bisector regression lines for the $M_{\rm BH}$–$M_{*,\rm sph}$ and $M_{\rm BH}$–$M_{*,\rm gal}$ relations over our total (reduced) sample of 76 ETGs (Figure 7) revealed two tight relations, which can be expressed as

$$\log(M_{\rm BH}/M_\odot) = (1.27 \pm 0.07)\log\left(\frac{M_{*,\rm sph}}{\upsilon(5 \times 10^{10}\,M_\odot)}\right) + (8.41 \pm 0.06), \qquad (10)$$

and

$$\log(M_{\rm BH}/M_\odot) = (1.65 \pm 0.11)\log\left(\frac{M_{*,\rm gal}}{\upsilon(5 \times 10^{10}\,M_\odot)}\right) + (8.02 \pm 0.08), \qquad (11)$$

with respective total rms scatters, in $\log(M_{\rm BH})$, of 0.52 dex and 0.58 dex.

The dark green line in both panels of Figure 7 represents the BCES bisector regression line for our sample of 76 ETGs, which is surrounded by a dark green shade showing the $\pm 1\sigma$ uncertainty in the slope and the intercept of the line. The light green shade represents the $\pm 1\sigma$ rms scatter of the data about the regression line.

The similarity in the scatter about both relations (Equations (10) and (11)) suggests that the black hole mass correlates nearly as well with galaxy stellar mass (or luminosity) as it does with spheroid stellar mass (or luminosity) for ETGs. This partly supports the claim of Läsker et al. (2014), albeit qualified by the restriction to ETGs as was noted by Savorgnan et al. (2016). Hence, with knowledge of the galaxy stellar mass, it would appear (at this stage of the analysis) that one can use the $M_{\rm BH}$–$M_{*,\rm gal}$ relation to estimate the black hole mass of an ETG nearly as accurately as if estimating it using the $M_{\rm BH}$–$M_{*,\rm sph}$ relation. Additionally, it should be remembered that a poor bulge/disk decomposition may introduce an error of noticeably more than 0.1 dex to the bulge stellar mass, and thus the $M_{\rm BH}$–$M_{*,\rm gal}$ relation may be preferable in many instances.

For our total galaxy stellar masses, we used a constant uncertainty of 0.12 dex (see Section 3.3) in all the regressions. However, we also derived the $M_{\rm BH}$–$M_{*,\rm gal}$ relation using a range of different uncertainties (0.10, 0.12, 0.15, 0.20 dex) on $\log M_{*,\rm gal}$, and found that the slope and intercept of Equation (11) remained within the $\pm 1\sigma$ bound.

Our scaling relations are based on the use of a different constant stellar mass-to-light ratio for each passband (see Table 1 and Section 3.3). However, we checked the robustness of our $M_{\rm BH}$–$M_{*,\rm sph}$ and $M_{\rm BH}$–$M_{*,\rm gal}$ relations by using the color-dependent stellar mass-to-light ratios to calculate galaxy and spheroid stellar masses for our galaxies. As explained in Section 3.4, we calculated $B - K_s$ color-dependent K_s-band stellar mass-to-light ratios ($\Upsilon_*^{K_s}$) for all our galaxies, using the equation $\log(\Upsilon_*^{K_s}) = 0.2119 \times (B - K_s) - 0.9586$ from Bell & de Jong (2001). Further, we used this $\Upsilon_*^{K_s}$ in the formulae from Oh et al. (2008) (Equation (3)) to obtain color-dependent $\Upsilon_*^{3.6\,\mu m}$. For the remaining two[15] SDSS r'-band images, we used $\Upsilon_*^{r'} = 2.8$,

---

[15] NGC 4486B, which is excluded from our regressions, is one of the three galaxies for which we used SDSS r'-band images.

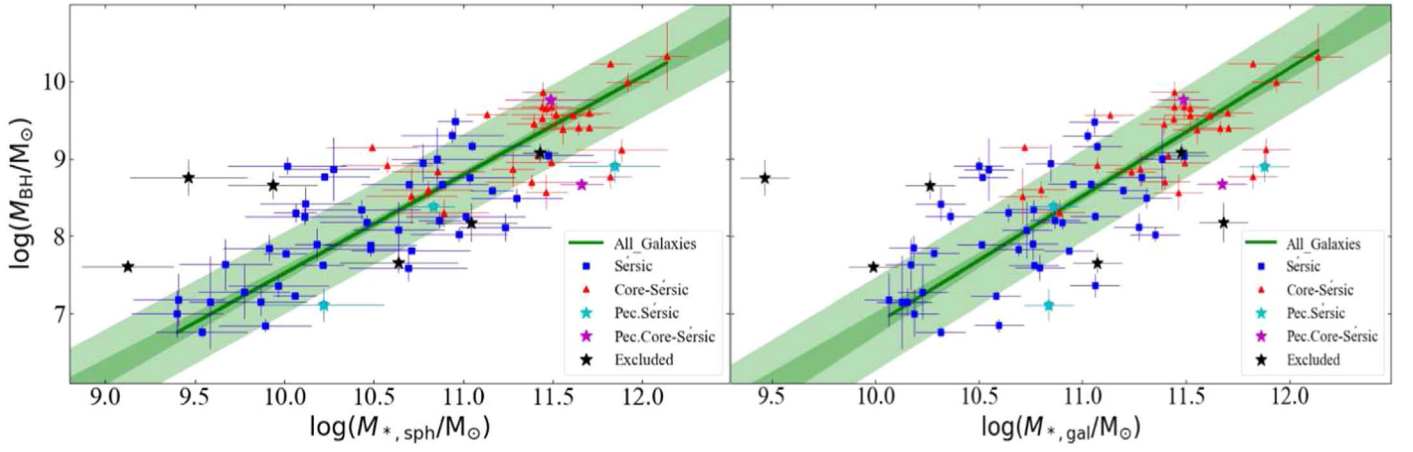**Figure 7.** Similar to Figure 6. The green lines represent the single bisector regression lines for the sample of (84–8=) 76 ETGs with $M_{BH} \gtrsim 10^7 M_{\odot}$. Both diagrams depict Sérsic and core-Sérsic ETGs following a unique relation in both the M_{BH}–$M_{*,sph}$ and M_{BH}–$M_{*,gal}$ diagrams, such that $M_{BH} \propto M_{*,sph}^{1.27\pm0.07}$ and $M_{BH} \propto M_{*,gal}^{1.65\pm0.11}$ with respective rms scatters of 0.52 dex and 0.58 dex (in the $\log M_{BH}$ direction).
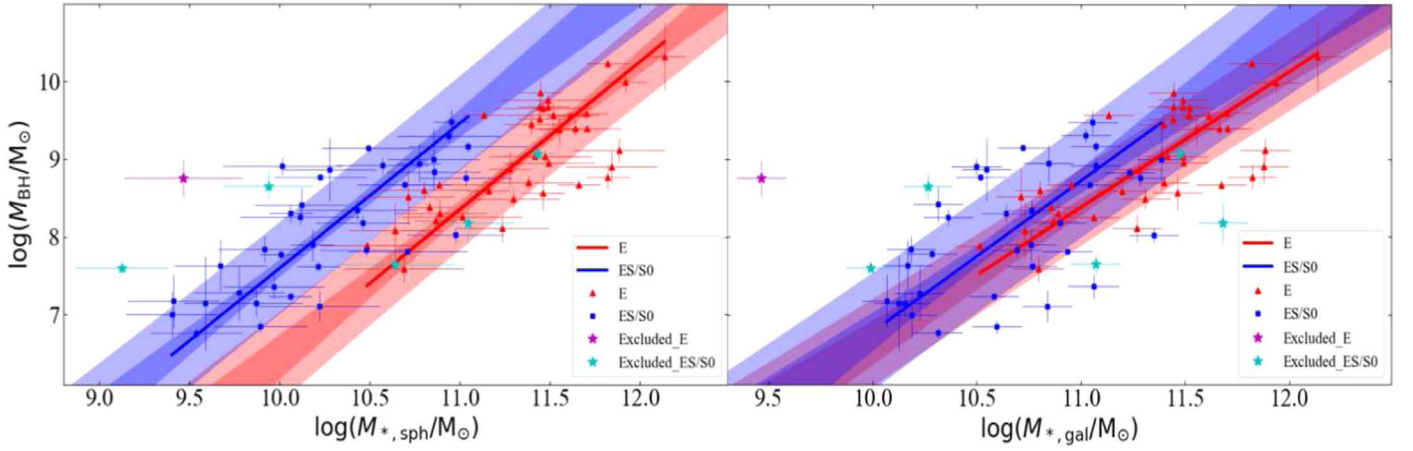

Figure 8. Similar to Figure 6, but now showing ETGs with (ES/S0) and without (E) a disk. In the M_{BH}–$M_{*,sph}$ diagram, the blue regression line for galaxies with a disk (blue squares) is offset from the red regression line for galaxies without a disk (red triangles) by more than an order of magnitude. This offset reveals two different scaling relations (Equations (12) and (13)) for the two submorphological types (ES/S0 and E) with rms scatters in the respective $\log(M_{BH})$ directions of 0.57 dex and 0.50 dex. In the M_{BH}–$M_{*,gal}$ diagram, both the regression lines (Equations (14) and (15)) are consistent with each other, suggesting a single relation (Equation (11)) for galaxies with and without disks.
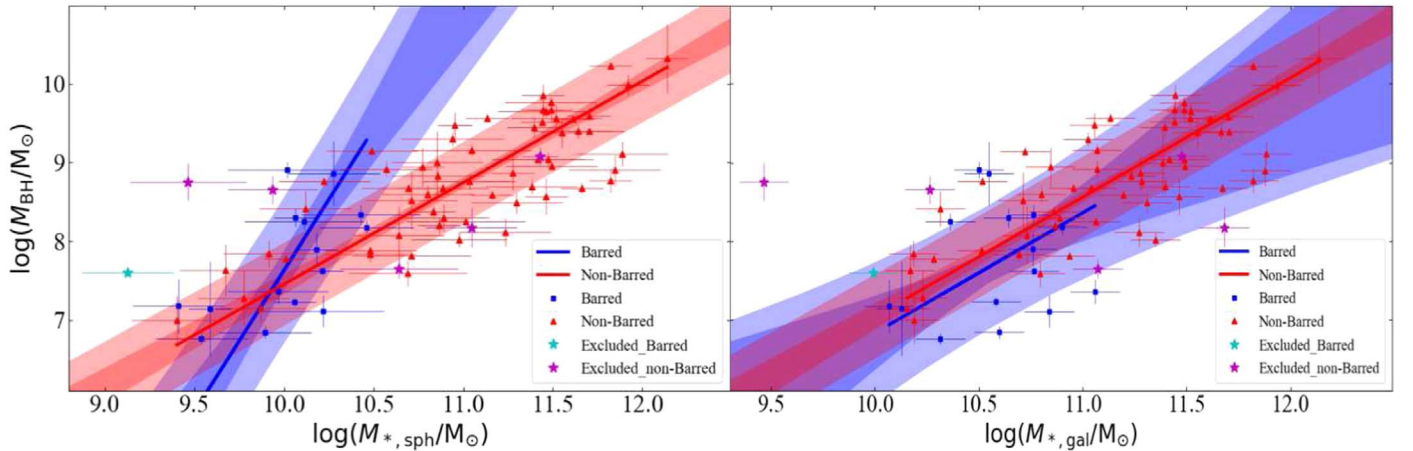

Figure 9. Similar to Figure 6, but now showing barred (15 blue squares) and non-barred (61 red triangles) galaxies. Upon performing separate regressions for galaxies with (blue line) and without (red line) bars, we found that the slopes of the two lines in the M_{BH}–$M_{*,gal}$ diagram are consistent (see Table 5), suggesting a single slope for barred and non-barred ETGs (see Figure 10). However, we require a larger data set of barred galaxies to draw a firm conclusion on whether or not barred galaxies create an offset in the M_{BH}–$M_{*,sph}$ relation.

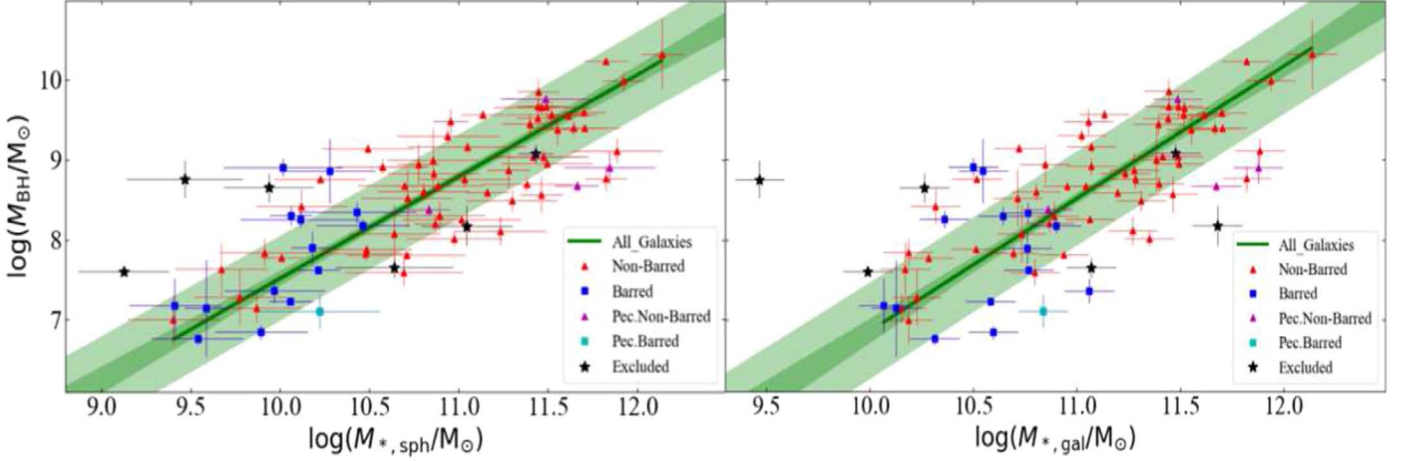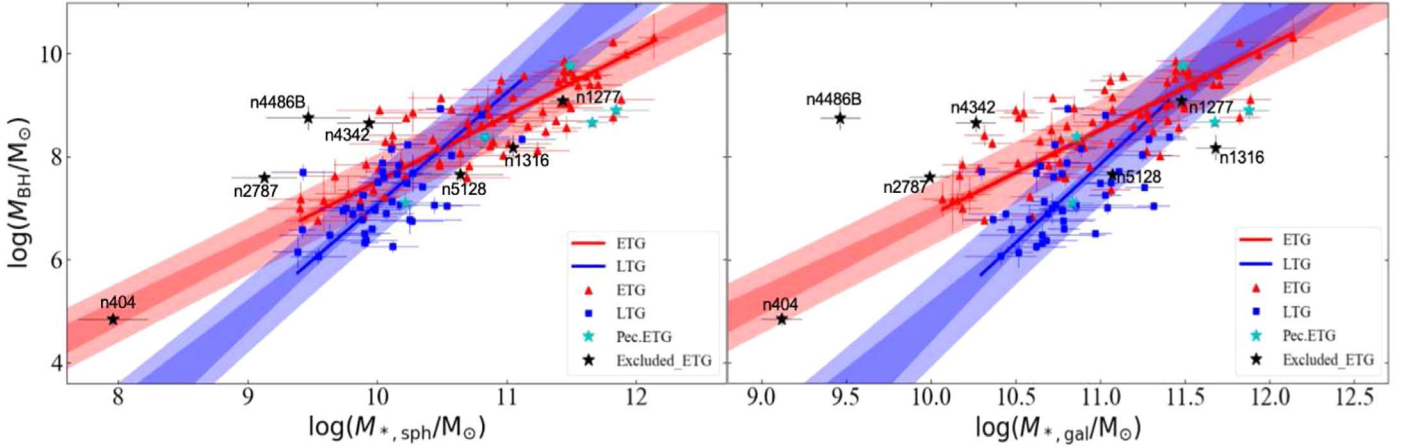**Figure 10.** Similar to Figure 7, but showing which galaxies are barred.

Figure 11. $M_{\rm BH}$–$M_{*,\rm sph}$ and $M_{\rm BH}$–$M_{*,\rm gal}$ relations for ETGs (red triangles) and LTGs (blue squares). Data for the late-type galaxies are taken from Davis et al. (2019). In both panels, the red and blue lines represent the bisector regression lines for ETGs and LTGs, respectively. In the $M_{\rm BH}$–$M_{*,\rm sph}$ diagram, $M_{\rm BH} \propto M_{*,\rm Sph}^{1.27\pm0.07}$ for ETGs and $M_{\rm BH} \propto M_{*,\rm Sph}^{2.17\pm0.32}$ for LTGs. In the $M_{\rm BH}$–$M_{*,\rm gal}$ diagram, $M_{\rm BH} \propto M_{*,\rm gal}^{1.65\pm0.11}$ for ETGs and $M_{\rm BH} \propto M_{*,\rm Gal}^{3.05\pm0.70}$ for LTGs. Although the ETG NGC 404 ($\log M_{\rm BH}/M\odot = 4.84$) is excluded from the regressions, it follows the regression lines for ETGs. NGC 4486B, which has the second-lowest galaxy stellar mass in our sample, is a stripped compact elliptical galaxy.

calibrated against 2MASS imaging as described in Section 3.3. The use of color-dependent stellar mass-to-light ratios for the spheroid and galaxy stellar masses of our sample resulted in $M_{\rm BH} \propto M_{*,\rm sph}^{1.20\pm0.07}$ and $M_{\rm BH} \propto M_{*,\rm sph}^{1.52\pm0.10}$. These relations are consistent within the $\pm1\sigma$ bound of our previous relations (Equations (10) and (11)) obtained using the masses based on the constant stellar mass-to-light ratios described in Section 3.3.

4.2. Galaxies with a Disk (ES/S0) and without a Disk (E)

We divided our ETG sample between those with an intermediate or extended disk (ES- and S0-type) and those without a disk (E-type), and performed separate BCES bisector regressions on each category. Figure 8 reveals separate relations for galaxies with a disk and galaxies without a disk in the $M_{\rm BH}$–$M_{*,\rm sph}$ diagram. The two relations are:

$$\log(M_{\rm BH}/M_\odot) = (1.86 \pm 0.20)\log\left(\frac{M_{*,\rm sph}}{\upsilon(5\times10^{10}M_\odot)}\right) + (8.90 \pm 0.13), \tag{12}$$

for 36 galaxies with a disk, and

$$\log(M_{\rm BH}/M_\odot) = (1.90 \pm 0.20)\log\left(\frac{M_{*,\rm sph}}{\upsilon(5\times10^{10}M_\odot)}\right) + (7.78 \pm 0.15), \tag{13}$$

for 40 galaxies without a disk, with rms scatters of 0.57 dex and 0.50 dex, respectively. While the slopes are consistent, the intercepts are different by 1.12 dex (more than an order of magnitude). Therefore, to estimate the black hole mass using the spheroid stellar mass of an ETG, it is beneficial to know whether the galaxy has a disk (ES/S0) or not (E).

In the $M_{\rm BH}$–$M_{*,\rm gal}$ diagram (Figure 8, right panel), the slopes of the regression lines for galaxies with (Equation (14)) and without (Equation (15)) a disk are again consistent. However, the intercepts of each relation now only differ by a factor of 2, rather than 13 (i.e., 1.12 dex), in black hole mass. While the 1σ uncertainty on these two intercepts does not quite overlap, we derive a single $M_{\rm BH}$–$M_{*,\rm gal}$ relation for ES/S0 and E-type galaxies. Given that one may not know whether their ETG of

Table 5
Linear Regressions

Regression (1)	Minimization (2)	α (3)	β (dex) (4)	ϵ (dex) (5)	$\Delta_{\rm rms}$ (dex) (6)	r (7)	$\log p$ (dex) (8)	r_s (9)	$\log p_s$ (dex) (10)
			76 Early-type Galaxies						
			$\log(M_{\rm BH}/M_\odot) = \alpha \log(M_{*,\rm sph}/[v(5 \times 10^{10}\,M_\odot)]) + \beta$						
BCES (*Bisector*)	*Symmetric*	1.27 ± 0.07	8.41 ± 0.06	0.41	0.52	0.82	−18.96	0.80	−17.20
BCES ($M_{\rm BH}|M_{*,\rm sph}$)	$M_{\rm BH}$	1.12 ± 0.08	8.43 ± 0.06	0.40	0.49				
BCES ($M_{*,\rm sph}|M_{\rm BH}$)	$M_{*,\rm sph}$	1.45 ± 0.09	8.38 ± 0.07	0.45	0.57				
			$\log(M_{\rm BH}/M_\odot) = \alpha \log(M_{*,\rm gal}/[v(5 \times 10^{10}\,M_\odot)]) + \beta$						
BCES (*Bisector*)	*Symmetric*	1.65 ± 0.11	8.02 ± 0.08	0.53	0.58	0.76	−15.12	0.76	−14.71
BCES ($M_{\rm BH}|M_{*,\rm gal}$)	$M_{\rm BH}$	1.33 ± 0.12	8.13 ± 0.08	0.51	0.55				
BCES ($M_{*,\rm gal}|M_{\rm BH}$)	$M_{*,\rm gal}$	2.10 ± 0.18	7.86 ± 0.11	0.63	0.69				
			Sérsic and Core-Sérsic Galaxies						
			45 Sérsic Galaxies: $\log(M_{\rm BH}/M_\odot) = \alpha \log(M_{*,\rm sph}/[v(5 \times 10^{10}\,M_\odot)]) + \beta$						
BCES (*Bisector*)	*Symmetric*	1.30 ± 0.14	8.43 ± 0.10	0.42	0.55	0.71	−7.34	0.71	−7.23
BCES ($M_{\rm BH}|M_{*,\rm sph}$)	$M_{\rm BH}$	1.05 ± 0.14	8.37 ± 0.09	0.40	0.50				
BCES ($M_{*,\rm sph}|M_{\rm BH}$)	$M_{*,\rm sph}$	1.63 ± 0.23	8.52 ± 0.13	0.49	0.66				
			31 Core-Sérsic Galaxies: $\log(M_{\rm BH}/M_\odot) = \alpha \log(M_{*,\rm sph}/[v(5 \times 10^{10}\,M_\odot)]) + \beta$						
BCES (*Bisector*)	*Symmetric*	1.38 ± 0.21	8.30 ± 0.20	0.43	0.50	0.56	−2.96	0.47	−2.11
BCES ($M_{\rm BH}|M_{*,\rm sph}$)	$M_{\rm BH}$	0.92 ± 0.27	8.62 ± 0.20	0.39	0.43				
BCES ($M_{*,\rm sph}|M_{\rm BH}$)	$M_{*,\rm sph}$	2.20 ± 0.55	7.72 ± 0.47	0.58	0.72				
			45 Sérsic Galaxies: $\log(M_{\rm BH}/M_\odot) = \alpha \log(M_{*,\rm gal}/[v(5 \times 10^{10}\,M_\odot)]) + \beta$						
BCES (*Bisector*)	*Symmetric*	1.61 ± 0.18	8.00 ± 0.09	0.59	0.63	0.58	−4.62	0.58	−4.52
BCES ($M_{\rm BH}|M_{*,\rm gal}$)	$M_{\rm BH}$	1.05 ± 0.17	8.04 ± 0.09	0.54	0.57				
BCES ($M_{*,\rm gal}|M_{\rm BH}$)	$M_{*,\rm gal}$	2.71 ± 0.55	7.93 ± 0.14	0.86	0.92				
			31 Core-Sérsic Galaxies: $\log(M_{\rm BH}/M_\odot) = \alpha \log(M_{*,\rm gal}/[v(5 \times 10^{10}\,M_\odot)]) + \beta$						
BCES (*Bisector*)	*Symmetric*	1.47 ± 0.18	8.17 ± 0.17	0.43	0.46	0.58	−3.22	0.48	−2.21
BCES ($M_{\rm BH}|M_{*,\rm gal}$)	$M_{\rm BH}$	0.96 ± 0.24	8.56 ± 0.18	0.39	0.42				
BCES ($M_{*,\rm gal}|M_{\rm BH}$)	$M_{*,\rm gal}$	2.44 ± 0.64	7.45 ± 0.55	0.62	0.68				
			Galaxies with a Disk (ES/S0) and Galaxies without a Disk (E)						
			36 Galaxies with a Disk (ES/S0): $\log(M_{\rm BH}/M_\odot) = \alpha \log(M_{*,\rm sph}/[v(5 \times 10^{10}\,M_\odot)]) + \beta$						
BCES (*Bisector*)	*Symmetric*	1.86 ± 0.20	8.90 ± 0.13	0.28	0.57	0.77	−7.39	0.77	−7.49
BCES ($M_{\rm BH}|M_{*,\rm sph}$)	$M_{\rm BH}$	1.70 ± 0.22	8.83 ± 0.14	0.29	0.54				
BCES ($M_{*,\rm sph}|M_{\rm BH}$)	$M_{*,\rm sph}$	2.05 ± 0.26	8.98 ± 0.15	0.29	0.62				
			40 Galaxies without a Disk (E): $\log(M_{\rm BH}/M_\odot) = \alpha \log(M_{*,\rm sph}/[v(5 \times 10^{10}\,M_\odot)]) + \beta$						
BCES (*Bisector*)	*Symmetric*	1.90 ± 0.20	7.78 ± 0.15	0.36	0.50	0.75	−7.63	0.70	−6.32
BCES ($M_{\rm BH}|M_{*,\rm sph}$)	$M_{\rm BH}$	1.68 ± 0.24	7.92 ± 0.15	0.34	0.46				
BCES ($M_{*,\rm sph}|M_{\rm BH}$)	$M_{*,\rm sph}$	2.16 ± 0.26	7.60 ± 0.21	0.39	0.56				
			36 Galaxies with a Disk (ES/S0): $\log(M_{\rm BH}/M_\odot) = \alpha \log(M_{*,\rm gal}/[v(5 \times 10^{10}\,M_\odot)]) + \beta$						
BCES (*Bisector*)	*Symmetric*	1.94 ± 0.21	8.14 ± 0.12	0.67	0.71	0.57	−3.52	0.56	−3.47
BCES ($M_{\rm BH}|M_{*,\rm gal}$)	$M_{\rm BH}$	1.26 ± 0.25	8.12 ± 0.11	0.62	0.64				
BCES ($M_{*,\rm gal}|M_{\rm BH}$)	$M_{*,\rm gal}$	3.47 ± 0.76	8.16 ± 0.18	1.01	1.08				
			40 Galaxies without a Disk (E): $\log(M_{\rm BH}/M_\odot) = \alpha \log(M_{*,\rm gal}/[v(5 \times 10^{10}\,M_\odot)]) + \beta$						
BCES (*Bisector*)	*Symmetric*	1.74 ± 0.16	7.85 ± 0.12	0.42	0.48	0.74	−7.28	0.70	−6.27
BCES ($M_{\rm BH}|M_{*,\rm gal}$)	$M_{\rm BH}$	1.38 ± 0.18	8.10 ± 0.12	0.40	0.45				
BCES ($M_{*,\rm gal}|M_{\rm BH}$)	$M_{*,\rm gal}$	2.27 ± 0.29	7.50 ± 0.24	0.51	0.58				
			Galaxies with and without a Bar						
			15 Galaxies with a Bar: $\log(M_{\rm BH}/M_\odot) = \alpha \log(M_{*,\rm sph}/[v(5 \times 10^{10}\,M_\odot)]) + \beta$						
BCES (*Bisector*)	*Symmetric*	3.59 ± 1.79	10.14 ± 1.15	0.34	0.86	0.60	−1.76	0.56	−1.53
BCES ($M_{\rm BH}|M_{*,\rm sph}$)	$M_{\rm BH}$	3.58 ± 2.40	10.13 ± 1.55	0.33	0.86				
BCES ($M_{*,\rm sph}|M_{\rm BH}$)	$M_{*,\rm sph}$	3.61 ± 1.37	10.15 ± 0.90	0.34	0.86				
			61 Galaxies without a Bar: $\log(M_{\rm BH}/M_\odot) = \alpha \log(M_{*,\rm sph}/[v(5 \times 10^{10}\,M_\odot)]) + \beta$						

Table 5
(Continued)

Regression	Minimization	α	β (dex)	ϵ (dex)	Δ_{rms} (dex)	r	$\log p$ (dex)	r_s	$\log p_s$ (dex)
(1)	(2)	(3)	(4)	(5)	(6)	(7)	(8)	(9)	(10)
BCES (*Bisector*)	*Symmetric*	1.29 ± 0.09	8.36 ± 0.07	0.41	0.51	0.78	−13.14	0.73	−10.78
BCES ($M_{\mathrm{BH}}|M_{*,\mathrm{sph}}$)	M_{BH}	1.10 ± 0.10	8.42 ± 0.07	0.39	0.47				
BCES ($M_{*,\mathrm{sph}}|M_{\mathrm{BH}}$)	$M_{*,\mathrm{sph}}$	1.52 ± 0.13	8.28 ± 0.10	0.46	0.58				
15 Galaxies with a Bar: $\log(M_{\mathrm{BH}}/M_\odot) = \alpha \log(M_{*,\mathrm{gal}}/[\upsilon(5 \times 10^{10}\,M_\odot)]) + \beta$									
BCES (*Bisector*)	*Symmetric*	1.52 ± 0.59	7.90 ± 0.22	0.73	0.73	0.18	−0.29	0.14	−0.20
BCES ($M_{\mathrm{BH}}|M_{*,\mathrm{gal}}$)	M_{BH}	0.53 ± 0.56	7.79 ± 0.18	0.67	0.67				
BCES ($M_{*,\mathrm{gal}}|M_{\mathrm{BH}}$)	$M_{*,\mathrm{gal}}$	13.19 ± 16.19	9.19 ± 1.56	3.41	3.51				
61 Galaxies without a Bar: $\log(M_{\mathrm{BH}}/M_\odot) = \alpha \log(M_{*,\mathrm{gal}}/[\upsilon(5 \times 10^{10}\,M_\odot)]) + \beta$									
BCES (*Bisector*)	*Symmetric*	1.52 ± 0.10	8.10 ± 0.08	0.46	0.50	0.78	−12.65	0.74	−11.05
BCES ($M_{\mathrm{BH}}|M_{*,\mathrm{gal}}$)	M_{BH}	1.23 ± 0.12	8.23 ± 0.08	0.44	0.48				
BCES ($M_{*,\mathrm{gal}}|M_{\mathrm{BH}}$)	$M_{*,\mathrm{gal}}$	1.90 ± 0.16	7.93 ± 0.11	0.54	0.59				
40 Late-type Galaxies									
$\log(M_{\mathrm{BH}}/M_\odot) = \alpha \log(M_{*,\mathrm{sph}}/[\upsilon(5 \times 10^{10}\,M_\odot)]) + \beta$									
BCES (*Bisector*)	*Symmetric*	2.16 ± 0.32	8.58 ± 0.22	0.48	0.64	0.66	−5.35	0.62	−4.62
BCES ($M_{\mathrm{BH}}|M_{*,\mathrm{sph}}$)	M_{BH}	1.70 ± 0.35	8.30 ± 0.22	0.46	0.56				
BCES ($M_{*,\mathrm{sph}}|M_{\mathrm{BH}}$)	$M_{*,\mathrm{sph}}$	2.90 ± 0.55	9.03 ± 0.39	0.59	0.82				
$\log(M_{\mathrm{BH}}/M_\odot) = \alpha \log(M_{*,\mathrm{gal}}/[\upsilon(5 \times 10^{10}\,M_\odot)]) + \beta$									
BCES (*Bisector*)	*Symmetric*	3.05 ± 0.70	6.93 ± 0.14	0.70	0.79	0.47	−2.70	0.53	−3.34
BCES ($M_{\mathrm{BH}}|M_{*,\mathrm{gal}}$)	M_{BH}	2.04 ± 0.72	7.04 ± 0.14	0.61	0.66				
BCES ($M_{*,\mathrm{gal}}|M_{\mathrm{BH}}$)	$M_{*,\mathrm{gal}}$	5.60 ± 1.57	6.66 ± 0.22	1.11	1.31				
ETGs with a disk (ES/S0), ETGs without a disk (E), and LTGs (Sp)									
36 Galaxies with a Disk (ES/S0): $\log(M_{\mathrm{BH}}/M_{*,\mathrm{sph}}) = \alpha \log(M_{*,\mathrm{sph}}/[\upsilon(5 \times 10^{10}\,M_\odot)]) + \beta$									
BCES (*Bisector*)	*Symmetric*	1.00 ± 0.14	−1.74 ± 0.12	0.46	0.60	0.25	−0.84	0.31	−1.17
40 Galaxies without a Disk (E): $\log(M_{\mathrm{BH}}/M_{*,\mathrm{sph}}) = \alpha \log(M_{*,\mathrm{sph}}/[\upsilon(5 \times 10^{10}\,M_\odot)]) + \beta$									
BCES (*Bisector*)	*Symmetric*	1.05 ± 0.11	−3.02 ± 0.12	0.45	0.53	0.23	−0.82	0.21	−0.69
40 Late-type Galaxies (Sp): $\log(M_{\mathrm{BH}}/M_{*,\mathrm{sph}}) = \alpha \log(M_{*,\mathrm{sph}}/[\upsilon(5 \times 10^{10}\,M_\odot)]) + \beta$									
BCES (*Bisector*)	*Symmetric*	1.22 ± 0.21	−2.08 ± 0.16	0.56	0.65	0.18	−0.56	0.18	−0.59
36 Galaxies with a Disk (ES/S0): $\log(M_{\mathrm{BH}}/M_{*,\mathrm{gal}}) = \alpha \log(M_{*,\mathrm{gal}}/[\upsilon(5 \times 10^{10}\,M_\odot)]) + \beta$									
BCES (*Bisector*)	*Symmetric*	1.12 ± 0.17	−2.56 ± 0.12	0.72	0.74	0.10	−0.25	0.12	−0.30
40 Galaxies without a Disk (E): $\log(M_{\mathrm{BH}}/M_{*,\mathrm{gal}}) = \alpha \log(M_{*,\mathrm{gal}}/[\upsilon(5 \times 10^{10}\,M_\odot)]) + \beta$									
BCES (*Bisector*)	*Symmetric*	1.07 ± 0.08	−3.06 ± 0.10	0.50	0.54	0.23	−0.83	0.21	−0.72
40 Late-type Galaxies (Sp): $\log(M_{\mathrm{BH}}/M_{*,\mathrm{gal}}) = \alpha \log(M_{*,\mathrm{gal}}/[\upsilon(5 \times 10^{10}\,M_\odot)]) + \beta$									
BCES (*Bisector*)	*Symmetric*	1.45 ± 0.66	−3.70 ± 0.14	0.67	0.70	0.12	−0.32	0.18	−0.56

Note. The data and linear regression for late-type galaxies are taken from Davis et al. (2019). Columns: (1) Regression performed. (2) The coordinate direction in which the offsets from the regression line is minimized. (3) Slope of the regression line. (4) Intercept of the regression line. (5) Intrinsic scatter in the M_{BH} direction (using Equation (1) from Graham & Driver (2007)). (6) Root mean square scatter in the M_{BH} direction. (7) Pearson correlation coefficient. (8) The Pearson correlation probability value. (9) Spearman rank-order correlation coefficient. (10) The Spearman rank-order correlation probability value.

interest contains a disk, one may prefer to estimate black hole mass using the total galaxy stellar mass via the relation obtained by performing the single regression (Equation (11)) on the whole sample of ETGs. The bisector regression line for the 36 ETGs with a disk is

$$\log(M_{\mathrm{BH}}/M_\odot) = (1.94 \pm 0.21)\log\left(\frac{M_{*,\mathrm{gal}}}{\upsilon(5 \times 10^{10} M_\odot)}\right)$$
$$+ (8.14 \pm 0.12), \qquad (14)$$

with an rms scatter of 0.71 dex. For the 40 galaxies without a disk, we obtained

$$\log(M_{\mathrm{BH}}/M_\odot) = (1.74 \pm 0.16)\log\left(\frac{M_{*,\mathrm{gal}}}{\upsilon(5 \times 10^{10} M_\odot)}\right)$$
$$+ (7.85 \pm 0.12), \qquad (15)$$

with an rms scatter of 0.48 dex.

The above results agree with the fact that most *elliptical* galaxies primarily consist of an extended spheroid; hence their total galaxy mass is nearly equal to their spheroid mass. Thus, in both the $M_{\rm BH}$–$M_{*,\rm sph}$ and $M_{\rm BH}$–$M_{*,\rm gal}$ diagrams, elliptical galaxies reside at the same place, usually at the high-mass end. The ellicular (ES) and lenticular (S0) galaxies have their total galaxy stellar mass distributed in their spheroid, disk, and sometimes other components. Therefore, their spheroid stellar mass can be significantly less than the galaxy stellar mass, and they reside at the low-mass (left) side of the $M_{\rm BH}$–$M_{*,\rm sph}$ diagram, creating an offset from the galaxies without a disk. We also performed BCES($Y|X$) and BCES($X|Y$) regressions for the above cases and the best-fit parameters can be found in Table 5.

4.3. Barred and Non-barred Galaxies

The $M_{\rm BH}$–σ relation is often reported to be the most fundamental relationship between the SMBH mass and any galaxy property, where σ is the velocity dispersion of the host galaxy's spheroid (Ferrarese & Merritt 2000; Gebhardt et al. 2000). However, previous studies have found that barred galaxies are offset toward higher σ values in the $M_{\rm BH}$–σ diagram (Graham 2007a, 2008; Graham et al. 2011). This offset can be accounted for in one of two ways: either the velocity dispersion of barred galaxies is systematically higher than non-barred galaxies (Hartmann et al. 2014), or their central SMBH mass is underestimated.

In an attempt to solve this problem, we performed separate regressions for the barred and non-barred galaxies in the $M_{\rm BH}$–$M_{*,\rm sph}$ and $M_{\rm BH}$–$M_{*,\rm gal}$ diagrams (see Figure 9). Our reduced sample of 76 ETGs consists of 15 barred galaxies (red squares) and 61 non-barred galaxies (blue triangles). The slopes of the $M_{\rm BH}$–$M_{*,\rm gal}$ relations for barred and non-barred ETGs are consistent with each other. However, with only 15 barred ETGs in our sample, the uncertainty on the slope of the $M_{\rm BH}$–$M_{*,\rm sph}$ relation for the barred galaxies is large (see Table 5), making it problematic to determine at what mass to compare the intercepts. From a visual inspection of Figure 9, we feel that it would be premature to draw any firm conclusion until more barred ETGs are in the sample.

The parameters of the BCES bisector, along with BCES($Y|X$) and BCES($X|Y$) regression lines for our data set of 15 barred and 61 non-barred ETGs, can be found in Table 5.

In Figure 10, we have again shown the single ETG regression line for both the $M_{\rm BH}$–$M_{*,\rm sph}$ and the $M_{\rm BH}$–$M_{*,\rm gal}$ relations (as in Figure 7), but here we identify the barred (blue squares) and non-barred (red triangles) galaxies with different symbols. The barred galaxies are not offset in the $M_{\rm BH}$–$M_{*,\rm gal}$ diagram, and there is no clear evidence for an offset to lower black hole masses in the $M_{\rm BH}$–$M_{*,\rm sph}$ diagram. This implies that the barred galaxies likely have a higher velocity dispersion relative to the non-barred galaxies, thereby creating the offset in the $M_{\rm BH}$–σ diagram.

4.4. ETGs and LTGs

We have combined our ETG data with the recent work on the largest sample of LTGs (i.e., spirals) with directly measured SMBH masses, by Davis et al. (2019). We found that the regression lines followed by these two populations, ETGs and LTGs,[16] in the $M_{\rm BH}$–$M_{*,\rm sph}$ and $M_{\rm BH}$–$M_{*,\rm gal}$ diagrams are not consistent with each other (see Figure 11).

In the black hole mass versus spheroid mass diagram, the regression line for the reduced sample of 40 LTGs from Davis et al. (2019) can be expressed as

$$\log(M_{\rm BH}/M_\odot) = (2.16 \pm 0.32)\log\left(\frac{M_{*,\rm sph}}{\upsilon(5 \times 10^{10} M_\odot)}\right) + (8.58 \pm 0.22), \qquad (16)$$

which has a slope approximately twice as steep as that of the ETGs: $M_{\rm BH} \propto M_{*,\rm sph}^{1.27 \pm 0.07}$ (Equation (10)). Similarly, in the black hole mass versus galaxy stellar mass diagram, LTGs define the relation

$$\log(M_{\rm BH}/M_\odot) = (3.05 \pm 0.70)\log\left(\frac{M_{*,\rm gal}}{\upsilon(5 \times 10^{10} M_\odot)}\right) + (6.93 \pm 0.14), \qquad (17)$$

while the ETGs follow the proportionality $M_{\rm BH} \propto M_{*,\rm gal}^{1.65 \pm 0.11}$ (Equation (11)).

This shallow and steep relation, for ETGs and LTGs, respectively, is roughly consistent with the bend observed by Savorgnan et al. (2016), where they found a near-linear relation, $M_{\rm BH} \propto M_{*,\rm sph}^{1.04 \pm 0.10}$, for their reduced[17] sample of 45 ETGs, with an rms scatter of 0.51 dex in the black hole mass, and $M_{\rm BH} \propto M_{*,\rm sph}^{2-3}$ for their 17 LTGs. They refer to the two correlations as an *early-type sequence* (or *red-type sequence*) and a *late-type sequence* (or *blue-type sequence*). Parameters for our BCES($Y|X$) and BCES($X|Y$) regression lines for LTGs and ETGs can be found in Table 5.

From our work, we infer that the previous papers found a bent $M_{\rm BH}$–$M_{*,\rm sph}$ relation due to Sérsic and core-Sérsic galaxies (e.g., Scott et al. 2013) because most of the Sérsic galaxies in their sample were LTGs and most of the core-Sérsic galaxies were ETGs. The bend in their relation was supposedly due to the different formation processes (dry merging versus gaseous growth), as traced by the difference in the central surface brightness profile of the galaxies. However, we find that the bend is due to the two broad morphological classes of galaxies: ETGs (consisting of ellipticals E, elliculars ES, and lenticulars S0) and LTGs (consisting of spirals Sp), supporting the finding in Savorgnan et al. (2016), which was later also shown by van den Bosch (2016); see his Figure 2.

The situation is, however, a little more complicated than presented above. As explained in Graham & Soria (2019), the color–magnitude relation for ETGs confound the situation when working with B-band magnitudes. This results in the fainter Sérsic ETGs following a steep B-band $M_{\rm BH}$–$L_{B,\rm sph}$ relation (and a shallow L_B–σ relation). Additionally, we have established that the bulges of ETGs follow a steep $M_{\rm BH}$–$M_{*,\rm sph}$ relation if one has a sample consisting of pure E-type or a sample of ES and S0 type. Section 8 reveals a slope of around 1.9 ± 0.2 for both of these populations, which is not overly dissimilar to the slope of 2.16 ± 0.32 for bulges in spiral galaxies.

Importantly, we find that the $(M_{\rm BH}/M_{*,\rm sph})$–$M_{*,\rm sph}$ and $(M_{\rm BH}/M_{*,\rm gal})$–$M_{*,\rm gal}$ relations (see Figure 12) are qualitatively and quantitatively consistent with our $M_{\rm BH}$–$M_{*,\rm sph}$ and $M_{\rm BH}$–$M_{*,\rm gal}$ relations for the subpopulations of ETGs (ES/S0 and E) and LTGs (Sp), within $\pm 1\sigma$ bound. Parameters for these regression lines can be found in Table 5. Figure 12 also depicts

---

[16] We have taken the BCES bisector regression line from Davis et al. (2018a).

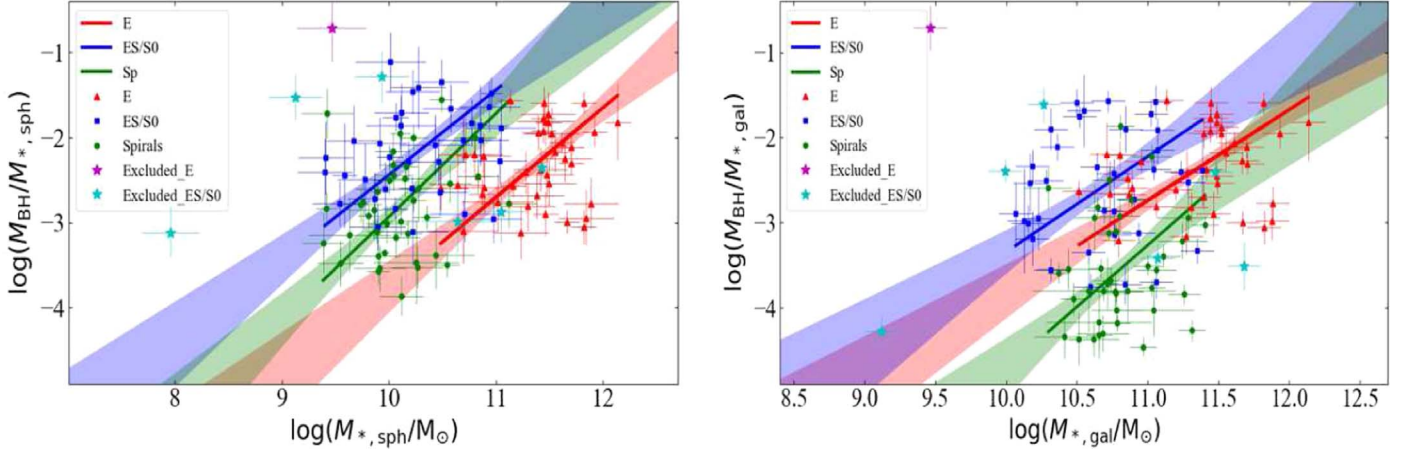[17] Savorgnan et al. (2016) excluded two ETGs and two LTGs from their total sample.

Figure 12. $(M_{BH}/M_{*,sph})$–$M_{*,sph}$ and $(M_{BH}/M_{*,gal})$–$M_{*,gal}$ relations for ETGs with a disk (blue squares), ETGs without a disk (red triangles), and LTGs (green circles). In both the panels, blue, red, and green lines represent the bisector regression lines for the three subpopulations of ES/S0-, E-, and Sp-type galaxies, respectively. Dark bands around the lines show the $\pm 1\sigma$ uncertainty in the corresponding slopes and intercepts. In the $(M_{BH}/M_{*,sph})$–$M_{*,sph}$ diagram, the regression line for ETGs with a disk is offset from the regression line for ETGs without a disk by 1.28 ± 0.17 dex in their $(M_{BH}/M_{*,sph})$ ratios, which is consistent with the offset observed in the M_{BH}–$M_{*,sph}$ diagram within the 1σ bound. In the $M_{BH}/M_{*,gal}$–$M_{*,gal}$ diagram, spiral galaxies follow steeper relation than ETGs, analogous to the right panel of Figure 11.

how the $M_{BH}/M_{*,sph}$ and $M_{BH}/M_{*,gal}$ ratios do not have a constant value, as was implied by our M_{BH}–$M_{*,sph}$ and M_{BH}–$M_{*,gal}$ relations.

4.5. NGC 5252: A Compact Massive Spheroid

In addition to the above scaling relations, we have discovered a compact massive spheroid in NGC 5252 ($z \approx 0.02$), with a stellar mass of $M_{*,sph} = 7.1^{+5.8}_{-3.2} \times 10^{10} M_\odot$ and a half-light radius ($R_{e,sph}$) of just 0.672 kpc, adding to the sample of 21 compact massive spheroid identified by Graham et al. (2015).

5. Conclusions and Implications

Our work, based on the largest sample of ETGs with directly measured SMBH masses, establishes a robust relation between the black hole mass and both the spheroid and galaxy stellar mass. While the color–magnitude relation for ETGs results in a steep M_{BH}–$L_{*,sph}$ relation in the optical bands for $MAG_{K_s} > -22$ mag, i.e., $B - K_s \leqslant 4.0$ (Graham & Soria 2019), the slopes at the low- and high-luminosity ends of the M_{BH}–$L_{*,sph}$ relation based on infrared magnitudes are equal to each other. That is, the M_{BH}–$M_{*,sph}$ relation for ETGs appears to be defined by a single log-linear relation. This helps to clarify debate over the existence of a steeper (at the low-mass end) and "bent" M_{BH}–$M_{*,sph}$ relation for ETGs.

Using our image reduction, profile extraction, and multi-component decomposition techniques, we carefully measured the spheroid and galaxy luminosities and stellar masses. We applied the BCES bisector regression to our data set, providing a symmetric treatment to both the M_{BH} and $M_{*,sph}$ or $M_{*,gal}$ data (we additionally report the scaling relations obtained from other asymmetric regressions in Table 5).

We checked the consistency of our M_{BH}–$M_{*,sph}$ and M_{BH}–$M_{*,gal}$ scaling relations by using stellar masses based on color-dependent stellar mass-to-light ratios, and found it to be in agreement with our scaling relations based on the constant stellar mass-to-light ratios. This may be partly due to our ETGs having fairly constant, red colors (Figure 5). Our key results can be summarized as follows:

1. Having performed separate regressions using 45 Sérsic and 31 core-Sérsic galaxies, we found that, for ETGs,

there is no significant bend in either the M_{BH}–$M_{*,sph}$ or M_{BH}–$M_{*,gal}$ diagram due to Sérsic and core-Sérsic galaxies (Figure 6).

2. ETGs follow a steep $M_{BH} \propto M_{*,sph}^{1.27\pm0.07}$ relation, with total rms scatter of 0.52 dex in the $\log M_{BH}$. The slope of this relation is nonlinear at the 3σ bound, leading us to the conclusion that a steeper-than-linear M_{BH}–$M_{*,sph}$ relation exists for ETGs. This also implies that the $M_{BH}/M_{*,sph}$ ratio is not a constant but varies along the relation.

3. The SMBH masses of ETGs follow an even steeper relation with the host *galaxy* stellar mass: $M_{BH} \propto M_{*,gal}^{1.65\pm0.11}$ with an rms scatter (in the $\log M_{BH}$ direction) of 0.58 dex. The slope of this relation is nonlinear at the 5.9σ level. The similarity between the rms scatter of this relation and that of the M_{BH}–$M_{*,sph}$ relation suggests that black hole mass correlates almost equally well with galaxy mass (luminosity) as it does with spheroid mass (luminosity) for ETGs (Figure 7). Hence, for the cases where bulge/disk decomposition is difficult, the M_{BH}–$M_{*,gal}$ relation can be used to estimate the black hole mass of an ETG by using the total galaxy stellar mass. However, as noted below, this approach is not preferred if one knows whether or not the ETG under study contains a disk.

4. We discovered separate relations for ETGs with an intermediate-scale or extended disk (ES or S0) and ETGs without a disk (E), having slopes 1.86 ± 0.20 and 1.90 ± 0.20 in the M_{BH}–$M_{*,sph}$ diagram, with an rms scatter in the $\log M_{BH}$ direction of 0.57 dex and 0.50 dex, respectively. Crucially, galaxies with a disk are offset from galaxies without a disk (Figure 8) by more than an order of magnitude (1.12 dex) in their $M_{BH}/M_{*,sph}$ ratio. This is likely due to the exclusion of the disk light, rather than an issue with the black hole mass. To better estimate the black hole mass of an ETG, one should use the corresponding M_{BH}–$M_{*,sph}$ relation depending on whether or not the ETG has a disk.

5. For the M_{BH}–$M_{*,gal}$ relation, the intercepts of the two regression lines (for galaxies with and without a disk) differ only by a factor of 2. Hence, the relation obtained by a single regression (Equation (11)) may still prove to be preferable for estimating the black hole mass when

uncertain about the presence of a disk in an ETG, or for those without a careful multicomponent decomposition.

6. We found that the regression lines for the barred galaxies (which reside at the lower-mass end of our diagrams) are largely consistent with the regression lines for the non-barred galaxies in both the $M_{\rm BH}$–$M_{*,\rm sph}$ and $M_{\rm BH}$–$M_{*,\rm gal}$ diagrams (Figures 9 and 10). However, with only 15 barred galaxies, it is too early to draw any firm conclusions. We restrict ourselves to noting that the barred galaxies do not appear to have lower SMBH masses than the non-barred galaxies in either the $M_{\rm BH}$–$M_{*,\rm sph}$ diagram or the $M_{\rm BH}$–$M_{*,\rm gal}$ diagram.

7. Combining the 76 ETGs studied here with the 40 LTGs from Davis et al. (2019), we observe a difference in the slope of the regression lines for ETGs and LTGs (Figure 11) in both the $M_{\rm BH}$–$M_{*,\rm sph}$ and $M_{\rm BH}$–M_{*gal} diagrams. The LTGs define steeper relations, such that $M_{\rm BH} \propto M_{*,\rm sph}^{2.17 \pm 0.32}$ and $M_{\rm BH} \propto M_{*,\rm gal}^{3.05 \pm 0.70}$. These slopes for the LTGs are almost double those of the ETGs. This agrees with the change noticed by Savorgnan et al. (2016) in the $M_{\rm BH}$–$M_{*,\rm sph}$ diagram.

8. We also found that the behavior of three subpopulations of galaxies (E, ES/S0, and Sp) in the $(M_{\rm BH}/M_{*,\rm sph})$–$M_{*,\rm sph}$ and $(M_{\rm BH}/M_{*,\rm gal})$–$M_{*,\rm gal}$ diagrams agree with the corresponding $M_{\rm BH}$–$M_{*,\rm sph}$ and $M_{\rm BH}$–$M_{*,\rm gal}$ relations (see Figures 8, 11, and 12), supporting the obvious implication of our nonlinear $M_{\rm BH}$ versus $M_{*,\rm sph}$ and $M_{*,\rm gal}$ scaling relations—specifically, that the $M_{\rm BH}/M_{*,\rm sph}$ and $M_{\rm BH}/M_{*,\rm gal}$ ratios are not constant.

The existence of substructure within the $M_{\rm BH}$–$M_{*,\rm sph}$ diagram, due to subpopulations of ETGs with and without disks, and spiral galaxy bulges, means that past efforts to calibrate the virial f-factor via the $M_{\rm BH}$–$M_{*,\rm sph}$ diagram—used for converting virial masses of active galactic nuclei into black hole masses (e.g., Bentz & Manne-Nicholas 2018)—will benefit from being revisited. Calibration of the offset between the ensemble of virial masses for AGNs and the ensemble of directly measured black hole masses should be performed separately, using the significantly different, nonlinear, $M_{\rm BH}$–$M_{*,\rm sph}$ relations for ETGs and LTGs, while taking into account the presence or absence of disks in the ETGs. A similar situation exists with the $M_{\rm BH}$–σ diagram, due to the offset subpopulations of galaxies with and without bars (Graham et al. 2011). In N. Sahu et al. (2019, in preparation), we will present an analysis of the $M_{\rm BH}$–σ relation based on the various subsamples of the ETG population used in this paper. We will also do this using our combined sample of 120 ETGs and LTGs.

Extending our search for the most fundamental black hole mass scaling relation, we will explore the correlation of black hole mass with the spheroid's Sérsic index[18] (n) and half light radius (R_e). We already have these two parameters from our homogeneous bulge/disk decomposition of ETGs and LTGs (Davis et al. 2019). We intend to check for the existence of a fundamental plane rather than a line. However, care needs to be taken, given that the L–R_e relation is curved (e.g., Graham & Worley 2008; A. Graham 2019, in preparation).

The black hole mass scaling relations presented in this work, based on a local ($z \approx 0$) sample of ETGs, can be used to estimate the black hole masses in other galaxies that do not have their SMBH's gravitational sphere-of-influence spatially resolved.

These scaling relations can be further used to derive the black hole mass function from the galaxy luminosity function, allowing the galaxy population to be separated according to morphological type for the first time. We plan to calculate the SMBH mass function by applying the black hole mass scaling relations for ETGs and LTGs to the updated spheroid and galaxy luminosity functions from GAMA data (Driver et al. 2009) for which the morphological types are known and bulge/disk decompositions have been performed.

The SMBH mass function, along with knowledge of the galaxy/SMBH merger rate, can be used to constrain the ground-based detection rate of long-wavelength gravitational waves, which are actively being searched for by the Parkes Pulsar Timing Array (Shannon et al. 2015; Hobbs & Dai 2017), the European Pulsar Timing Array (Stappers & Kramer 2011), and the North American Nanohertz Observatory for Gravitational Waves (NANOGrav, Siemens 2019). Using the forthcoming SMBH mass function, we intend to improve the predictions for the detection of the gravitational waves from PTA and make new predictions for detection from the recently inaugurated MeerKAT telescope (Jonas 2007). The revised black hole scaling relations can also be used to predict the detection of gravitational waves from future space-based detectors. For example, Mapelli et al. (2012) investigate the detection of gravitational waves produced from the merger of SMBHs with stellar-mass BHs and neutron stars in the central nuclear star clusters of galaxies (Hartmann 2011).

ORCID iDs

Nandini Sahu ⬤ https://orcid.org/0000-0003-0234-6585
Alister W. Graham ⬤ https://orcid.org/0000-0002-6496-9414
Benjamin L. Davis ⬤ https://orcid.org/0000-0002-4306-5950

References

Abbott, B. P., Abbott, R., Abbott, T. D., et al. 2016, ApJL, 818, L22
Adelman-McCarthy, J. K., Agüeros, M. A., Allam, S. S., et al. 2008, ApJS, 175, 297
Aihara, H., Allende Prieto, C., An, D., et al. 2011, ApJS, 193, 29
Akritas, M. G., & Bershady, M. A. 1996, ApJ, 470, 706
Almoznino, E., Loinger, F., & Brosch, N. 1993, MNRAS, 265, 641
Anglés-Alcázar, D., Faucher-Giguère, C.-A., Quataert, E., et al. 2017, MNRAS, 472, L109
Athanassoula, E. 2002, ApJL, 569, L83
Athanassoula, E. 2005, MNRAS, 358, 1477
Baes, M., Buyle, P., Hau, G. K. T., & Dejonghe, H. 2003, MNRAS, 341, L44
Batcheldor, D., Axon, D., Valluri, M., Mandalou, J., & Merritt, D. 2013, AJ, 146, 67
Batcheldor, D., Robinson, A., Axon, D. J., Perlman, E. S., & Merritt, D. 2010, ApJL, 717, L6

---

[18] The Sérsic index is a measure of the radial concentration of stellar mass.

Begelman, M. C., Blandford, R. D., & Rees, M. J. 1980, Natur, 287, 307
Begelman, M. C., & Nath, B. B. 2005, MNRAS, 361, 1387
Belczynski, K., Bulik, T., Fryer, C. L., et al. 2010, ApJ, 714, 1217
Bell, E. F., & de Jong, R. S. 2001, ApJ, 550, 212
Bentz, M. C., & Manne-Nicholas, E. 2018, ApJ, 864, 146
Bertin, E., & Arnouts, S. 1996, A&AS, 117, 393
Blanton, M. R., Schlegel, D. J., Strauss, M. A., et al. 2005, AJ, 129, 2562
Blom, C., Forbes, D. A., Foster, C., Romanowsky, A. J., & Brodie, J. P. 2014, MNRAS, 439, 2420
Bonfini, P., González-Martín, O., Fritz, J., et al. 2018, MNRAS, 478, 1161
Bonoli, S., Mayer, L., & Callegari, S. 2014, MNRAS, 437, 1576
Buson, L. M., Bertola, F., Bressan, A., Burstein, D., & Cappellari, M. 2004, A&A, 423, 965
Capak, P. L., Teplitz, H. I., Brooke, T. Y., Laher, R., & Science Center, S. 2013, AAS Meeting Abstracts, 221, 340.06
Capetti, A., Marconi, A., Macchetto, D., & Axon, D. 2005, A&A, 431, 465
Carter, D., Bridges, T. J., & Hau, G. K. T. 1999, MNRAS, 307, 131
Carter, D., & Jenkins, C. R. 1993, MNRAS, 263, 1049
Chabrier, G. 2003, PASA, 115, 763
Ciambur, B. C. 2015, ApJ, 810, 120
Ciambur, B. C. 2016, PASA, 33, e062
Ciotti, L. 1991, A&A, 249, 99
Cirasuolo, M., Shankar, F., Granato, G. L., De Zotti, G., & Danese, L. 2005, ApJ, 629, 816
Combes, F., & Sanders, R. H. 1981, A&A, 96, 164
Conroy, C., Gunn, J. E., & White, M. 2009, ApJ, 699, 486
Courteau, S., Cappellari, M., de Jong, R. S., et al. 2014, RvMP, 86, 47
Coziol, R., Andernach, H., Caretta, C. A., Alamo- Martínez, K. A., & Tago, E. 2009, AJ, 137, 4795
Cretton, N., & van den Bosch, F. C. 1999, ApJ, 514, 704
Croton, D. J., Springel, V., White, S. D. M., et al. 2006, MNRAS, 365, 11
Dalla Bontà, E., Ferrarese, L., Corsini, E. M., et al. 2009, ApJ, 690, 537
Davis, B. L., Graham, A. W., & Cameron, E. 2018a, ApJ, 869, 113
Davis, B. L., Graham, A. W., & Cameron, E. 2019, ApJ, 873, 85
Davis, T. A., Bureau, M., Onishi, K., et al. 2018b, MNRAS, 473, 3818
de Vaucouleurs, G. 1969, ApL, 4, 17
de Vaucouleurs, G., de Vaucouleurs, A., Corwin, H. G., et al. 1991, Third Reference Catalogue of Bright Galaxies (New York: Springer)
Diamond-Stanic, A. M., & Rieke, G. H. 2012, ApJ, 746, 168
Di Matteo, T., Colberg, J., Springel, V., Hernquist, L., & Sijacki, D. 2008, ApJ, 676, 33
D'Onofrio, M., Zaggia, S. R., Longo, G., Caon, N., & Capaccioli, M. 1995, A&A, 296, 319
Dressler, A., & Richstone, D. O. 1988, ApJ, 324, 701
Dressler, A. 1989, in IAU Symp., Active Galactic Nuclei, ed. D. E. Osterbrock & J. S. Miller (Dordrecht: Kluwer), 217
Driver, S. P., Norberg, P., Baldry, I. K., et al. 2009, A&G, 50, 12
Drouart, G., De Breuck, C., Vernet, J., et al. 2014, A&A, 566, A53
Dubois, Y., Devriendt, J., Slyz, A., & Teyssier, R. 2012, MNRAS, 420, 2662
Dullo, B. T., & Graham, A. W. 2014, MNRAS, 444, 2700
Elbert, O. D., Bullock, J. S., & Kaplinghat, M. 2018, MNRAS, 473, 1186
Erwin, P., Saglia, R. P., Fabricius, M., et al 2015, MNRAS, 446, 4039
Erwin, P., Thomas, J., Saglia, R. P., et al. 2018, MNRAS, 473, 2251
Escudero, C. G., Faifer, F. R., Bassino, L. P., Calderón, J. P., & Caso, J. P. 2015, MNRAS, 449, 612
Fabian, A. C. 1999, MNRAS, 308, L39
Falcón-Barroso, J., Peletier, R. F., Emsellem, E., et al. 2004, MNRAS, 350, 35
Fedorova, E., Vasylenko, A., Hnatyk, B. I., & Zhdanov, V. I. 2016, AN, 337, 96
Ferrarese, L. 2002, ApJ, 578, 90
Ferrarese, L., Cote, P., Blakeslee, J. P., et al. 2006, arXiv:astro-ph/0612139
Ferrarese, L., & Ford, H. 2005, SSRv, 116, 523
Ferrarese, L., & Merritt, D. 2000, ApJL, 539, L9
Ferrers, N. M. 1877, QJPAM, 14, 1
Fontanot, F., Monaco, P., Cristiani, S., & Tozzi, P. 2006, MNRAS, 373, 1173
Gadotti, D. A., & Kauffmann, G. 2009, MNRAS, 399, 621
Gadotti, D. A., Seidel, M. K., Sánchez- Blázquez, P., et al. 2015, A&A, 584, A90
Gebhardt, K., Bender, R., Bower, G., et al. 2000, ApJL, 539, L13
Gebhardt, K., Richstone, D., Tremaine, S., et al. 2003, ApJ, 583, 92
Gould, A. 2013, arXiv:1303.0834
Graham, A. 2007a, AAS Meeting Abstracts, 211, 13.27
Graham, A. W. 2002, ApJL, 568, L13
Graham, A. W. 2004, ApJL, 613, L33
Graham, A. W. 2007b, MNRAS, 379, 711
Graham, A. W. 2008, PASA, 25, 167

Graham, A. W. 2012, ApJ, 746, 113
Graham, A. W. 2016, ASSL, 418, 263
Graham, A. W., Ciambur, B. C., & Savorgnan, G. A. D. 2016a, ApJ, 831, 132
Graham, A. W., & Driver, S. P. 2005, PASA, 22, 118
Graham, A. W., & Driver, S. P. 2007, ApJ, 655, 77
Graham, A. W., Dullo, B. T., & Savorgnan, G. A. D. 2015, ApJ, 804, 32
Graham, A. W., Durré, M., Savorgnan, G. A. D., et al. 2016b, ApJ, 819, 43
Graham, A. W., Erwin, P., Trujillo, I., & Asensio Ramos, A. 2003, AJ, 125, 2951
Graham, A. W., Onken, C. A., Athanssoula, E., & Combes, R. MNRAS, 412, 2211
Graham, A. W., & Scott, N. 2013, ApJ, 764, 151
Graham, A. W., & Scott, N. 2015, ApJ, 798, 54
Graham, A. W., & Soria, R. 2019, MNRAS, 484, 794
Graham, A. W., Soria, R., & Davis, B. L. 2019, MNRAS, 484, 814
Graham, A. W., & Worley, C. C. 2008, MNRAS, 388, 1708
Gültekin, K., Richstone, D. O., Gebhardt, K., et al. 2009a, ApJ, 698, 198
Gültekin, K., Richstone, D. O., Gebhardt, K., et al. 2009b, ApJ, 695, 1577
Hailey, C. J., Mori, K., Bauer, F. E., et al. 2018, Natur, 556, 70
Halliday, C. 1998, PhD thesis
Hartmann, M. 2011, PhD thesis, Univ. Central Lancashire
Hartmann, M., Debattista, V. P., Cole, D. R., et al. 2014, MNRAS, 441, 1243
Hirano, S., Hosokawa, T., Yoshida, N., & Kuiper, R. 2017, Sci, 357, 1375
Ho, L. 1999, ASSL, 234, 157
Hobbs, G., & Dai, S. 2017, arXiv:1707.01615
Hopkins, P. F., Hernquist, L., Cox, T. J., et al. 2006, ApJS, 163, 1
Hu, J. 2008, MNRAS, 386, 2242
Inayoshi, K., & Haiman, Z. 2016, ApJ, 828, 110
Jarrett, T. H., Chester, T., Cutri, R., Schneider, S. E., & Huchra, J. P. 2003, AJ, 125, 525
Jedrzejewski, R. I. 1987a, MNRAS, 226, 747
Jedrzejewski, R. I. 1987b, in IAU Symp. 127, Structure and dynamics of ellpiptical galaxies (Dordrecht: Reidel), 37
Jiang, F., van Dokkum, P., Bezanson, R., & Franx, M. 2012, ApJL, 749, L10
Jonas, J. 2007, From Planets to Dark Energy: the Modern Radio Universe, 7
Kannappan, S. J., & Gawiser, E. 2007, ApJL, 657, L5
Khandai, N., Feng, Y., DeGraf, C., Di Matteo, T., & Croft, R. A. C. 2012, MNRAS, 423, 2397
Kormendy, J. 2000, HST Proposal, 8687
Kormendy, J., & Bender, R. 2012, ApJS, 198, 2
Kormendy, J., Bender, R., & Cornell, M. E. 2011, Natur, 469, 374
Kormendy, J., Bender, R., Magorrian, J., et al. 1996, AAS Meeting Abstracts, 189, 111.01
Kormendy, J., & Ho, L. C. 2013, ARA&A, 51, 511
Kormendy, J., & Richstone, D. 1995, ARA&A, 33, 581
Krajnović, D., Cappellari, M., McDermid, R. M., et al. 2018, MNRAS, 477, 3030
Krajnović, D., McDermid, R. M., Cappellari, M., & Davies, R. L. 2009, MNRAS, 399, 1839
Kuo, C. Y., Braatz, J. A., Condon, J. J., et al. 2011, ApJ, 727, 20
Laine, S., van der Marel, R. P., Lauer, T. R., et al. 2003, AJ, 125, 478
LaMassa, S. M., Heckman, T. M., Ptak, A., & Urry, C. M. 2013, ApJL, 765, L33
Laor, A. 1998, ApJL, 505, L83
Laor, A. 2001, ApJ, 553, 677
Läsker, R., Ferrarese, L., van de Ven, G., & Shankar, F. 2014, ApJ, 780, 70
Laurikainen, E., Salo, H., & Buta, R. 2005, MNRAS, 362, 1319
Laurikainen, E., Salo, H., Buta, R., & Knapen, J. H. 2007, MNRAS, 381, 401
Laurikainen, E., Salo, H., Buta, R., & Knapen, J. H. 2009, ApJL, 692, L34
Laurikainen, E., Salo, H., Buta, R., & Knapen, J. H. 2011, MNRAS, 418, 1452
Levine, D., Wu, X., Good, J., et al. 2009, in ASP Conf. Ser. 411, adass XVIII, ed. D. Bohlender, P. Durand, & P. Dowler (San Francisco, CA: ASP), 29
Liller, M. H. 1966, ApJ, 146, 28
Longo, G., Zaggia, S. R., Busarello, G., & Richter, G. 1994, A&AS, 105, 433
Lynden-Bell, D. 1969, Natur, 223, 690
Lynden-Bell, D., & Rees, M. J. 1971, MNRAS, 152, 461
Magorrian, J., Tremaine, S., Richstone, D., et al. 1998, AJ, 115, 2285
Mapelli, M. 2016, MNRAS, 459, 3432
Mapelli, M., Ripamonti, E., Vecchio, A., Graham, S. W., & Gualandris, A. 2012, A&A, 542, A102
Marconi, A., Risaliti, G., Gilli, R., et al. 2004, MNRAS, 351, 169
Martinez-Valpuesta, I., Knapen, J. H., & Buta, R. 2007, AJ, 134, 1863
Martín-Navarro, I., La Barbera, F., Vazdekis, A., et al. 2015, MNRAS, 451, 1081
Mayer, L., Kazantzidis, S., Madau, P., et al. 2007, Sci, 316, 1874
Mazzalay, X., Thomas, J., Saglia, R. P., et al. 2016, MNRAS, 462, 2847

21

McConnell, N. J., Ma, C.-P., Graham, J. R., et al. 2011, ApJ, 728, 100
Meidt, S. E., Schinnerer, E., van de Ven, G., et al. 2014, ApJ, 788, 144
Merritt, D. 2006, MmSAI, 77, 750
Mezcua, M. 2017, IJMPD, 26, 1730021
Miller, M. C. 2003, in AIP Conf. Ser. 686, The Astrophysics of Gravitational Wave Sources, ed. J. M. Centrella (Melville, NY: AIP), 125
Mitchell, P. D., Lacey, C. G., Baugh, C. M., & Cole, S. 2013, MNRAS, 435, 87
Moffat, A. F. J. 1969, A&A, 3, 455
Morganti, R. 2017, FrASS, 4, 42
Muñoz-Mateos, J. C., Sheth, K., Gil de Paz, A., et al. 2013, ApJ, 771, 59
Muñoz-Mateos, J. C., Sheth, K., Gil de Paz, A., et al. 2016, ApJ, 818, 101
Natarajan, P., & Treister, E. 2009, MNRAS, 393, 838
Natarajan, P., & Volonteri, M. 2012, MNRAS, 422, 2051
Neistein, E., & Netzer, H. 2014, MNRAS, 437, 3373
Nemmen, R. S., Georganopoulos, M., Guiriec, S., et al. 2012, Sci, 338, 1445
Nguyen, D. D., Seth, A. C., den Brok, M., et al. 2017, ApJ, 836, 237
Oh, S.-H., de Blok, W. J. G., Walter, F., Brinks, E., & Kennicutt, R. C., Jr. 2008, AJ, 136, 2761
Onishi, K., Iguchi, S., Davis, T. A., et al. 2017, MNRAS, 468, 4663
Pignatelli, E., Salucci, P., & Danese, L. 2001, MNRAS, 320, 124
Planck Collaboration, Aghanim, N., Akrami, Y., et al. 2018, arXiv:1807.06209
Press, W. H., Teukolsky, S. A., Vetterling, W. T., & Flannery, B. P. 1992, Numerical Recipes in FORTRAN. The Art of Scientific Computing (Cambridge: Cambridge Univ. Press)
Querejeta, M., Meidt, S. E., Schinnerer, E., et al. 2015, ApJS, 219, 5
Quillen, A. C., Bower, G. A., & Stritzinger, M. 2000, ApJS, 128, 85
Reines, A. E., Sivakoff, G. R., Johnson, K. E., & Brogan, C. L. 2011, Natur, 470, 66
Richings, A. J., Uttley, P., & Körding, E. 2011, MNRAS, 415, 2158
Roediger, J. C., & Courteau, S. 2015, MNRAS, 452, 3209
Rubin, V. 1995, HST Proposal, 6002
Rusli, S. P., Erwin, P., Saglia, R. P., et al. 2013a, AJ, 146, 160
Rusli, S. P., Thomas, J., Saglia, R. P., et al. 2013b, AJ, 146, 45
Sabra, B. M., Saliba, C., Abi Akl, M., & Chahine, G. 2015, ApJ, 803, 5
Saglia, R. P., Opitsch, M., Erwin, P., et al. 2016, ApJ, 818, 47
Saha, K., Graham, A. W., & Rodríguez-Herranz, I. 2018, ApJ, 852, 133
Salo, H., Laurikainen, E., Laine, J., et al. 2015, ApJS, 219, 4
Salucci, P., Ratnam, C., Monaco, P., & Luigi, D. 2000, MNRAS, 317, 488
Sandage, A. 1961, The Hubble Atlas of Galaxies (Washington, DC: Carnegie Institute)
Sani, E., Marconi, A., Hunt, L. K., & Risaliti, G. 2011, MNRAS, 413, 1479
Sarzi, M., Rix, H.-W., Shields, J. C., et al. 2001, ApJ, 550, 65
Satyapal, S., Secrest, N. J., McAlpine, W., et al. 2014, ApJ, 784, 113
Savorgnan, G. A. D., & Graham, A. W. 2016a, ApJS, 222, 10

Savorgnan, G. A. D., & Graham, A. W. 2016b, MNRAS, 457, 320
Savorgnan, G. A. D., Graham, A. W., Marconi, A., & Sani, E. 2016, ApJ, 817, 21
Scharwächter, J., McGregor, P. J., Dopita, M. A., & Beck, T. L. 2013, MNRAS, 429, 2315
Schombert, J., & Smith, A. K. 2012, PASA, 29, 174
Schramm, M., Silverman, J. D., Greene, J. E., et al. 2013, ApJ, 773, 150
Schulze, A., & Gebhardt, K. 2011, ApJ, 729, 21
Scott, N., Graham, A. W., & Schombert, J. 2013, ApJ, 768, 76
Secrest, N. J., Satyapal, S., Gliozzi, M., et al. 2012, ApJ, 753, 38
Seigar, M. S., Graham, A. W., & Jerjen, H. 2007, MNRAS, 378, 1575
Sérsic, J. L. 1963, BAAA, 6, 41
Seymour, N., Altieri, B., De Breuck, C., et al. 2012, ApJ, 755, 146
Shankar, F., Bernardi, M., Sheth, R. K., et al. 2016, MNRAS, 460, 3119
Shankar, F., Weinberg, D. H., & Miralda-Escudé, J. 2009, ApJ, 690, 20
Shannon, R. M., Ravi, V., Lentati, L. T., et al. 2015, Sci, 349, 1522
Shen, J., & Gebhardt, K. 2010, ApJ, 711, 484
Sheth, K., Regan, M., Hinz, J. L., et al. 2010, PASP, 122, 1397
Siemens, X. 2019, AAS Meeting Abstracts, 233, 149.24
Simmons, B. D., Lintott, C., Schawinski, K., et al. 2013, MNRAS, 429, 2199
Springel, V., White, S. D. M., Jenkins, A., et al. 2005, Natur, 435, 629
Stappers, B., & Kramer, M. 2011, AAS Meeting Abstracts, 217, 124.04
Taylor, E. N., Hopkins, A. M., Baldry, I. K., et al. 2011, MNRAS, 418, 1587
Thomas, J., Ma, C.-P., McConnell, N. J., et al. 2016, Natur, 532, 340
Tolman, R. C. 1930, PNAS, 16, 511
Tremaine, S., Gebhardt, K., Bender, R., et al. 2002, ApJ, 574, 740
Trujillo, I., Erwin, P., Asensio Ramos, A., & Graham, A. W. 2004, AJ, 127, 1917
van den Bosch, R. C. E. 2016, ApJ, 831, 134
van der Marel, R. P., & van den Bosch, F. C. 1998, AJ, 116, 2220
Walsh, J. L., Barth, A. J., Ho, L. C., & Sarzi, M. 2013, ApJ, 770, 86
Walsh, J. L., van den Bosch, R. C. E., Gebhardt, K., et al. 2017, ApJ, 835, 208
Wandel, A. 1999, ApJL, 519, L39
Wolfe, A. M., & Burbidge, G. R. 1970, ApJ, 161, 419
Wu, X., Roby, T., & Ly, L. 2010, in ASP Conf. Ser. 434, adass XIX, ed. Y. Mizumoto, K.-I. Morita, & M. Ohishi (San Francisco, CA: ASP), 14
Wyithe, J. S. B., & Loeb, A. 2003, ApJ, 595, 614
Yang, X., Yang, J., Paragi, Z., et al. 2017, MNRAS, 464, L70
Yee, H. K. C. 1992, in ASP Conf. Ser. 31, Relationships Between Active Galactic Nuclei and Starburst Galaxies, ed. A. V. Filippenko (San Francisco, CA: ASP), 417
Yıldırım, A., van den Bosch, R. C. E., van de Ven, G., et al. 2015, MNRAS, 452, 1792
York, D. G., Adelman, J., Anderson, J. E., Jr., et al. 2000, AJ, 120, 1579